Volume 3, Issue 2, 2020
e-ISSN: 2667-484X

KOCAELI UNIVERSITY
1992

KOCAELI JOURNAL OF SCIENCE AND ENGINEERING

http://dergipark.org.tr/kojose
kojose@kocaeli.edu.tr

Owner

Prof. Dr. Sadettin HÜLAGÜ - (Kocaeli University)

Editor in Chief

Prof. Dr. K. Süleyman YİĞİT - (Kocaeli University)

Associate Editors

Assoc. Prof. Dr. H. Hakan GÜREL - (Kocaeli University)
Assoc. Prof. Dr. Mihriban CİVAN (Kocaeli University)
Prof. Dr. Murat HOŞÖZ - (Kocaeli University)
Asst. Prof. Dr. Recep Kaya GÖKTAŞ (Kocaeli University)

Production Editors

R. A. Abdurrahman GÜN - (Kocaeli University)
Instructor Yusuf YAĞCI - (Kocaeli University)

Copy Editor (English)

Lecturer Ķsmail HakkēPASLI - (Kocaeli University)

Assistant Editors

R. A. Abdurrahman GÜN - (Kocaeli University)
R. A. Alp Eren ŞAHİN - (Kocaeli University)

Secretary

Durmuк ĶMAT - (Kocaeli University)

Section Editors

Prof. Dr. Adnan SÖZEN (Gazi University)
Assoc. Prof. Dr. Ahmet SAYAR (Kocaeli University)
Prof. Dr. Ahmet Ziyaettin ŞAHİN (KFUPM, S.A.)
Asst. Prof. Dr. Alaattin Metin KAYA (Bursa Uludağ University)
Prof. Dr. Aleksandrs SOSTAKS (University of Latvia)
Prof. Dr. Ata ATUN (Cyprus Science University)
Asst. Prof. Dr. Atakan ALKAN (Kocaeli University)
Prof. Dr. Ayşe Nilgün AKIN (Kocaeli University)
Prof. Dr. Beyhan PEKEY (Kocaeli University)
Prof. Dr. Bülent ORUÇ (Kocaeli University)
Prof. Dr. Cihan KARAKUZU (Bilecik Şeyh Edebali University)
Prof. Dr. Dong LI (Northeast Petroleum University)
Asst. Prof. Dr. Emre KİSHALI (Kocaeli University)
Prof. Dr. Engin ÖZDEMİR (Kocaeli University)
Prof. Dr. Erhan PULAT (Bursa Uludağ University)
Prof. Dr. Fatma GÜLTEKİN (Karadeniz Technical University)
Prof. Dr. Günay ÖZTÜRK (İzmir Demokrasi University)
Prof. Dr. Hamid EL-QARNIA (Cadi Ayyad University)
Dr. Helena AZEVEDO (Queen Mary University of London)
Prof. Dr. Hüseyin Metin ERTUNÇ (Kocaeli University)
Prof. Dr. Iulian STANASEL (University of Oradea)
Prof. Dr. Kamaruzzaman SOPIAN (The National University of Malaysia)
Assoc. Prof. Dr. Kerem KÜÇÜK (Kocaeli University)
Prof. Dr. Mehmet ARIK (Özyeğin University)
Assoc. Prof. Dr. Mehmet Ufuk KASIM (Kocaeli University)
Asst. Prof. Dr. Mihriban CİVAN (Kocaeli University)
Prof. Dr. Mustafa ÇANAKCI (Kocaeli University)
Assoc. Prof. Dr. Müslüm ARICI (Kocaeli University)
Prof. Dr. Nilgün FIĞLALI (Kocaeli University)
Prof. Dr. Nurhan Turgut DUNFORD (Oklahoma State University)
Prof. Dr. Oscar CASTILLO (Tijuana Institute of Technology)
Asst. Prof. Dr. Recep Kaya GÖKTAŞ (Kocaeli University)
Asst. Prof. Dr. Suhap ŞAHİN (Kocaeli University)
Prof. Dr. Tahsin ENGİN (Sakarya University)
Prof. Dr. Tamer SINMAZÇELİK (Kocaeli University)
Prof. Dr. Recep Taygun GÜRAY (Kocaeli University)
Assoc. Prof. Dr. Wang FUQIANG (Harbin Institute of Technology)
Prof. Dr. Yunus Emre ERDEMLİ (Kocaeli University)
Prof. Dr. Zerrin ALADAĞ (Kocaeli University)

Advisory Board

Assoc. Prof. Dr. Ahmet KARAKAŞ (Kocaeli University)
Prof. Dr. Ali KILIÇARSLAN (Hitit University)
Prof. Dr. Ali SÜRMEN (Uludağ University)
Asst. Prof. Dr. Ayşe Arzu ARI (Kocaeli University)
Assoc. Prof. Dr. Burcu ONAT (Istanbul University)
Asst. Prof. Dr. Canan Dilek EREN (Kocaeli University)
Prof. Dr. Cenk SAYIN (Marmara University)
Prof. Dr. Fadime SERTÇELIK (Kocaeli University)
Prof. Dr. Feriha Erfan KUYUMCU (Kocaeli University)
Assoc. Prof. Dr. Halil YİĞİT (Kocaeli University)
Assoc. Prof. Dr. Halim Aytekin ERGÜL (Kocaeli University)
Prof. Dr. Hasan KÜRÜM (Fırat University)
Assoc. Prof. Dr. Hikmet SÜRMELİ (Mersin University)
Assoc. Prof. Dr. İlyas KANDEMIR (Gebze Technical University)
Assoc. Prof. Dr. Kasım BAYNAL (Kocaeli University)
Prof. Dr. Mehmet YILMAZ (Kocaeli University)
Assoc. Prof. Dr. Murat Selim ÇEPNİ (Kocaeli University)
Prof. Dr. Nevim GENÇ (Kocaeli University)
Prof. Dr. Nil Pembe ÖZER (Kocaeli University)
Prof. Dr. Oğuzhan URHAN (Kocaeli University)
Assoc. Prof. Dr. Onur ÇOBAN (Kocaeli University)
Prof. Dr. Özcan GÜNDOĞDU (Kocaeli University)
Prof. Dr. Raşit KÖKER (Sakarya University)
Prof. Dr. Rezzan KASIM (Kocaeli University)
Prof. Dr. Safa Bozkurt ÇOŞKUN (Kocaeli University)
Prof. Dr. Serdar İPLİKÇİ (Pamukkale University)
Prof. Dr. Sezai TOKAT (Pamukkale University)
Assoc. Prof. Dr. Şaban Hakan ATAPEK (Kocaeli University)
Prof. Dr. Şeref Naci ENGİN (Yıldız Technical University)
Assoc. Prof. Dr. Vildan ÇETKİN (Kocaeli University)

Printed By

Kocaeli University - Graduate School of Natural and Applied Sciences - Umuttepe Campus 41380, Kocaeli / TURKEY
Tel: +090 (262) 303 35 56 Fax: +090 (262) 303 30 33 E-mail: kojose@kocaeli.edu.tr

Koc. J. Sci. Eng., 3(2): (2020) 33-40 https://doi.org/10.34088/kojose.657462

Kocaeli University

Kocaeli Journal of Science and Engineering

http://dergipark.org.tr/kojose

Numerical Examination of Heat Transfer Augmentation between the Plates with Square Cross-Sectional Ribs for the Staggered Arrangement

Ilker Goktepeli [1, *], Ulas Atmaca [2]

[1] *Department of Mechanical Engineering, Konya Technical University, Konya, 42075, Turkey,* ***ORCID:*** *0000-0002-2886-8018*
[2] *Department of Mechanical Engineering, Konya Technical University, Konya, 42075, Turkey,* ***ORCID:*** *0000-0002-9265-1446*

Article Info

Research paper

Received : December 10, 2019
Accepted : October 15, 2020

Keywords

CFD
Nusselt Number
Parallel Plate
Reynolds Number
Rib
Turbulent Fow

Abstract

Heat transfer enhancement in the ducts is significantly related with flow separation and reattachment regions. Therefore, ribs are used to obtain the rotational flows in the vicinity of the wall since the fluctuations in the thermal and hydrodynamic boundary layers are effective for the increment of heat transfer by convection. Even though heat transfer surface area is enlarged by placing the ribs into the channels, the pressure loss due to the ribs has to be taken into account and controlled in these systems. Based on the aforementioned explanations, the square cross-sectional ribs have been mounted on the bottom and the top walls of horizontal parallel plates in terms of staggered arrangement. In the present paper, numerical analyses have been conducted via k-ω SST turbulence model at Re = 10000, 15000 and 20000 for different spacing values between two successive ribs. For the constant rib dimensions, the ribbed models have been compared by referring to smooth plates as reference model. For this reason; time-averaged results including streamwise velocity components, temperature distributions, pressure values, streamline patterns and Nusselt numbers for the ribbed and the smooth plates have been separately presented and compared. Heat transfer has been enhanced due to the ribs deforming the hydrodynamic and thermal boundary layers. Furthermore, increasing the rib spacing and Reynolds number has enhanced Nusselt number. As observed, heat transfer has also been augmented by extending the distance between two successive ribs since fluid easily penetrates to the sink between them for the production of recirculation regions. However, in case of the ribbed models, there are gradual drop pressure values along the channel. For this reason, the rib effect on these values is much more as evidently observed at Re = 10000.

1. Introduction

Heat transfer augmentation via passive methods is an important subject in the engineering. The power expenditure reduction of the system is considered when it comes to improve thermal performance.

Even though high-performance cooling or heating units requiring less cooling working fluid are aimed in the design process, momentum and heat transfer in ribbed channels is not a straightforward problem as expected [1]. The main target is to enhance the amount of convective heat transfer by implementing various techniques. All passive techniques are almost applied by extending the wetted surface area via artificial surface elements. Moreover, it is done by breaking of both hydrodynamic and thermal boundary layers. In this context, a rib is a surface element to increase both heat transfer and turbulence intensity. A method for passive heat transfer enhancement has been carried out [2] to disrupt velocity and temperature profiles near to the plates for the generation of recirculation regions around the surface elements. It is known that the vortices lean to move by tracking swirling paths causing the fluid displacement between the core regions and the plates [3]. Thus, the amount of heat transfer via convection is augmented by directing more fresh fluid onto the plates [4]. Local heat transfer coefficient is increased as stated in these cases. In

---

[*] Corresponding Author: igoktepeli@ktun.edu.tr

This article is an extended version of the paper presented at the 22nd Congress on Thermal Science and Technology.

this study, for this reason, the square ribs have been mounted on the plates. Although various kinds of vortex generators were used in the previous studies [5−8], the rectangular element is one of the most frequently used ribs. Since the rib shape is important for the effect of heat transfer enhancement, its orientations and arrangements are accepted as effective on the thermal performance. As explained [9], the rib shape and its arrangement cause the separation bubble and the fluctuations related with the turbulent kinetic energy. On that account, staggered arrangement has been preferred in the present study. The staggered ribs have been placed on the plates to improve the thermal efficiency as in the similar approach proposed [10]. Staggered rib configuration is feasible for the thermal systems requiring periodical flow conditions as discussed [11]. Successive studies including the staggered arrangement with the rectangular cross-sectional ribs have been done [12−16]. In some studies [17−20], the staggered arrangement has been contrasted with the symmetrical one. Accordingly, the aim of this numerical study is to investigate heat transfer enhancement between the plates in terms of the staggered arrangement.

2. Numerical Method

2.1. Boundary and Initial Conditions

In this study, the square cross-sectional ribs have been mounted on the plates by considering the staggered arrangement. Heat transfer enhancement owing to the ribs has been investigated via k-ω SST turbulence model for two-dimensional analyses between the horizontal plates. ANSYS Fluent 18.0 has been used for the numerical analyses. One of the ribbed models used has been presented in Figure 1.

The channel height, H, is 0.05 m. The hydraulic diameter is $D_H = 2H$. All dimensions have been normalized with the duct height, L' = L/H = 20, as done for the length of the channel. The height and the width of the rib are shown as h' = h/H = 0.1 and w' = w/H = 0.1, respectively, which are constant for this study. The spacing between two ribs on the same plate is from S' = S/H = 0.5 to 1. Moreover, the rib on any plate has been centered with respect to the two successive ribs of the opposite plate as indicated in Figure 1. The ribs have been mounted after L' = 10 for the flow development [21]. Four models have been used in the present study.

Heat transfer and turbulent flow characteristics between the horizontal plates have been numerically investigated for $10000 \leq Re = U_\infty D_H / \nu \leq 20000$ where the inlet velocity values are 0.1 m/s $\leq U\infty \leq 0.2$ m/s. Thermophysical properties of fluid flow have been assumed to be constant for the numerical analyses.

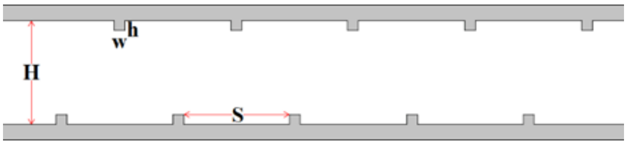

Figure 1. The schematic of the model.

Four models have been formed for the numerical analyses. In the next step, it is needed to attain the proper grid structure for the solution process. The boundary conditions for the study have been given in Figure 2. Uniform velocity which is normal to the boundary has been used at the inlet of the channel. Pressure outlet with gauge pressure of zero has been defined at the outlet which is open to atmosphere. In the regions where the fluid contacts the wall, no-slip boundary condition has been applied. For the smooth plate, in the case that no rib is used, wall boundary condition is identified for the plates. In case of the ribbed plate, the same boundary condition has been implemented for surfaces having the ribs which are in contact with the fluid.

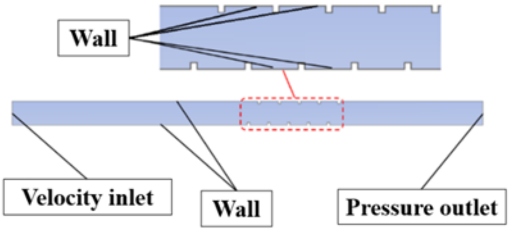

Figure 2. Boundary conditions.

Due to the incompressible flow, pressure-based solver has been utilized. Semi-Implicit Method for Pressure-Linked Equations (SIMPLE) scheme has been used for the pressure-velocity coupling.

2.2. Grid Structure

Various parameters are related with generation of the grid structure. In this manner, a correlation for the smooth plate has been considered for the comparison with the numerical result as given in Eq. (1) [22]. The solution has to be independent of the grid structure.

$$Nu = 0.021\, Pr^{0.5} Re^{0.8} \tag{1}$$

As a result of this correlation, Nusselt number has been calculated as Nu = 84.19 at Re = 10000. Firstly, the results of the smooth plate have been compared with the result of the correlation for Re = 10000 via four turbulence models. Exemplarily, the results of the turbulence models have been presented in Table 1. The closest result to the result of the correlation has been obtained by k-ω Shear Stress Transport (SST) turbulence model. The second one was standard k-ω turbulence model. Although better results have been acquired via two k-ω turbulence models, k-ω SST turbulence model has been approved because of the nearest result to the correlation result. Furthermore, the numerical analyses including smooth plates have been verified by comparing the Nusselt numbers with the ones of the considered correlation. After the validation of the results, the numerical analyses for the ribbed plates have been maintained and then completed.

Table 1. Prototype electric vehicle parameters.

Turbulence model	**Nu**
k-ε Realizable	97.63
k-ε Re-Normalization Group (RNG)	115.37
k-ω Shear Stress Transport (SST)	86.43
k-ω Standard	87.55

Nusselt numbers have been found via k-ω SST turbulence model based on different grid numbers as shown in Table 2. Even though the results were very close to each other for all grid structures, the nearest result with regard to the correlation has been provided via the grid number of 6.6×10^5.

Table 2. Nusselt numbers attained for different grid numbers via k-ω SST turbulence model at Re = 10000.

Grid number	**Nu**
3×10^5	87.01
4.3×10^5	86.46
6.6×10^5	86.43
8.6×10^5	86.52
1.16×10^6	86.53

The skewness (maximum value ≤ 0.95) and the orthogonal quality (minimum value ≥ 0.15) values have been obtained as in the suggested intervals [23]. A meshed model has been indicated with the detailed views in Figure 3.

Figure 3. The meshed model given as an example.

Thinner grid elements have been formed in the walls containing the ribs to take the boundary layer effect into account. Edge sizing for the grid structure has been used and the total thickness inflation has been applied for the first ten layers.

2.3. Equations

Based on the number of the grid structure and the proper turbulence model determined for the present study, all numerical analyses have been conducted with the software solver. It is needed to underscore that the solver equations are very crucial in the background. In the flow modeling, continuity and momentum equations have been solved. In case of the turbulent flow, Reynolds-Averaged Navier-Stokes (RANS) equations are obtained with the time-averaged versions of these equations. For the incompressible flow condition, the continuity and the momentum equations have been given with Eqs. (2-3, respectively [23]. In these equations, k stands for the turbulent kinetic energy and ω represents the specific dissipation rate. Moreover, $\widetilde{G}_k$ is the generation of the turbulent kinetic energy owing to the average velocity gradients while G_ω is defined as the generation of the specific dissipation rate. The effective diffusivity values of k and ω are symbolized with Γ_k and Γ_ω terms. Also, Y_k and Y_ω are the dissipation of k and ω due to turbulence. The cross-diffusion term is given by D_ω while S_k and Sω are the user-defined source terms.

$$\frac{\partial \overline{u_i}}{\partial x_i} = 0 \tag{2}$$

$$\frac{\partial \bar{u}_i}{\partial t} + \frac{\partial(\bar{u}_i \bar{u}_j)}{\partial x_j} = -\frac{1}{\rho}\frac{\partial \bar{p}}{\partial x_i} - \frac{\partial \tau_{ij}}{\partial x_j} + \frac{\partial}{\partial x_j}\left(\nu \frac{\partial \bar{u}_i}{\partial x_j}\right) \tag{3}$$

Energy equation, presented in Eq. (4), is solved for the heat transfer problems [23]:

$$\frac{\partial}{\partial t}(\rho E) + \frac{\partial}{\partial x_i}[u_i(\rho E + p)] = \frac{\partial}{\partial x_j}\left[\left(k + \frac{C_p \mu_t}{Pr_t}\right)\frac{\partial T}{\partial x_j} + u_i(\tau_{ij})_{eff}\right] + S_h \tag{4}$$

Additional terms, the turbulent stresses, have to be included in the solution procedure enabled by the turbulence model. The equations used in the turbulence model have been presented in Eqs. (5-6) [23]:

$$\frac{\partial}{\partial t}(\rho k) + \frac{\partial}{\partial x_i}(\rho k u_i) = \frac{\partial}{\partial x_j}\left[\Gamma_k \frac{\partial k}{\partial x_j}\right] + \widetilde{G}_k - Y_k + S_k \ \# \tag{5}$$

$$\frac{\partial}{\partial t}(\rho \omega) + \frac{\partial}{\partial x_i}(\rho \omega u_i) = \frac{\partial}{\partial x_j}\left[\Gamma_\omega \frac{\partial \omega}{\partial x_j}\right] + G_\omega - Y_\omega + D_\omega + S_\omega \ \# \tag{6}$$

In the numerical analyses, the time step was 0.0068 s and maximum twenty iterations per time step have been done. Nonetheless, the total number of the iterations changes with the required analysis duration depending on the residuals of the equations as 10^{-8} for all analyses. As a result, the dimensionless wall distance has been provided as $y+ = u^* y/\nu \cong 1$ and matched with the criteria.

3. Results and Discussion

Heat transfer characteristics attained by performing the numerical analyses between the parallel plates have been presented for $10000 \leq Re \leq 20000$ in Figures 4–7. These considered characteristics have been given for time-averaged results of temperature <T> and pressure <P> distributions, streamwise velocity components <u> and streamline patterns <Ψ>. Mean Nusselt number values (Nu) have also been given in Figure 8.

Time-averaged results of temperature <T> distributions have been attained as a result of the numerical analyses and indicated in Figure 4. Fluid at 300 K has been assumed to enter the duct and its plates were at 400 K. The maximum and the minimum values were as 400 K and 300 K, respectively for the problem including the single-phase flow. Since the temperature distributions have been differently obtained for different ducts, changes of the heat transfer characteristics are clearly observed. However, there is less effect of the smooth plate on heat transfer as compared to that of the ribbed models. This is due to temperature variation observed close to the wall. In this case, heat transfer is enhanced by increasing Reynolds number since heat transfer coefficient is augmented as a result of the increment of the flow rate. For this reason, the rib effect on the heat transfer characteristics is much more. Due to the interaction between fluid flow and ribs, there is flow separation owing to the first one. As mentioned before, heat transfer enhancement is done since increasing Reynolds number causes the increment of heat transfer coefficient. This is explained by the breaking of hydrodynamic and thermal boundary layers because of the ribs. In these regions, the sudden temperature changes are observed due to chaotic flow. Heat transfer has been considerably increased as stated. This mentioned situation has been observed for all cases. Increase in fluid temperature has been provided along the centerline of the duct owing to the increment of the rib heights. Moreover, heat transfer surface area has been enlarged by the ribs. This also causes augmentation of heat transfer. Though mounting the higher rib to increase the influence of the flow separation in terms of the heat transfer augmentation, the rib height is restricted by the distance between the opposite plates. What is more, pressure loss has to be considered in the design of the heat transfer equipment. In such condition, as an alternative parameter, the spacing between the ribs is taken into account for heat transfer enhancement. As observed from the results, heat transfer has been enhanced by enlarging the gap between two successive ribs since fluid easily penetrates to the space between them for the production of recirculation regions. This aforementioned situation has been seen from the temperature change as given in Figure 4. Increasing the spacing between the ribs also extends the contact area for the fluid after the flow reattachment. In case of narrow spacing between the ribs, it is challenging for the fluid to enter to the zone between the ribs. It can be seen from Figure 4 that only one circulation zone occurs when the ribs are closer enough to each other. While the distance is increased, two circulation zones can be seen and this phenomenon increases the heat transfer coefficient. The temperature contours (Figure 4) and streamline distributions (Figure 7) exhibit similar patterns as can be seen from the aforementioned graphics.

Time-averaged results of pressure distributions have been given in Figure 5 as a result of the numerical analyses performed. Pressure loss for the smooth plate was less than the ribbed model as expected for all Reynolds numbers. In case of the model with no ribs, there is gradual drop observed for pressure values along the channel as anticipated again. However, pressure loss values have increased because of increasing Reynolds number. In the meantime, placing the ribs on the plates also triggers the pressure drop. For the same rib spacing, increase in Reynolds number causes pressure loss as observed. By keeping Reynolds number constant at Re = 10000, there is not much change observed in pressure values for different rib spacing values. However, pressure loss has been triggered by increasing the spacing between the ribs for Reynolds numbers of Re = 15000 and Re = 20000. Moreover, there is sharp decrement in pressure seen for all cases with the ribbed plates. This region that sudden decrease of pressure values occurred is generally the wake of the first rib on the upper plate. Especially, this is the minimum pressure region for $S' = 0.5$ at $10000 \leq Re \leq 20000$. When the rib spacing was gradually increased, the additional minimum pressure zones have been observed in the wake regions of different ribs depending on their position. After the second ribs, pressure values have increased and approached to the mean values of the legend bar. Temporary recovery for pressure values has been attained. This situation is related with the decrease of flow rate after the second ribs. The recovery in pressure occurred earlier for the cases of $S' = 0.5$ and kept its disposition until the outlet of the ribbed region. However, there is again a decrement for pressure in the vicinity of the last rib on the lower plate. After the ribbed region passed, mean pressure values have been provided.

Time-averaged results of streamwise velocity components <u> have been indicated in Figure 6. For the smooth plates, the maximum values of the velocity components have been obtained at the exterior region of boundary layer. Due to no-slip condition on the wall, there is decrease in the velocity components in the regions under the thumb of boundary layer. Since there are no turbulators on the plates, rotational flow has not been acquired. As can be seen from the charts, the cross-sectional flow area of the channel is minimized owing to the ribs placed on the plates. These ribs have caused the flow separation as well as rotational flow. For this reason, negative velocity values have been obtained in terms of the ribbed ducts. Therefore, there is an increment for the streamwise velocity components observed due to the increment of the rib height values. This phenomenon is explained via flow separation owing to the first rib on both plates. Due to the staggered rib arrangement, asymmetrical flow patterns have been observed. In case of the forward-facing step flow where after the flow separates from the walls, it reattaches to the upstream corner of the rib and it is again separated from that point. In the regions where flow is separated, the rotational flows have been seen at the upstream of the rib. This is identified as the forward-facing step flow in the front of the rib, the cavity flow between two successive ribs and the backward-facing step flow in the wake region of the rib [24]. In terms of the cavity flow; rotational flow, which is more energetic between the first two ribs relatively, has lost its influence between the other ones. For most of the cases, the regions where the maximum values attained in were the sinks bounded by the first two ribs and the upper side of the centerline. However, there is not much change for the streamwise velocity components while the margin between the ribs is widened. The region that the maximum values are achieved has also been sighted between the other ribs depending on increment of rib spacing.

Time-averaged results of streamline patterns <Ψ> have been given in Figure 7 as a result of the numerical analyses performed. In terms of the smooth plates, uniform flow has been observed since there are no additional elements diminishing the flow. In the presence of the ribs, rather chaotic flow structure has been obtained. Flow structure has changed with increasing rib spacing. Rotational flow has been seen between first two ribs in a row due to flow separation considerably affected by them. Since the leading element to distort the flow was the first rib, larger vortices have been attained in the wake of the first one for both plates. The separated flow produces a lower pressure region at the downstream of the first ribs as in Figure 7. Periodical flow has been seen because of the rib arrangement; the intensity of eddies was less than the first ones. What is more, the required distance for the flow recovery is approximately constant for the rib spacing and Reynolds number.

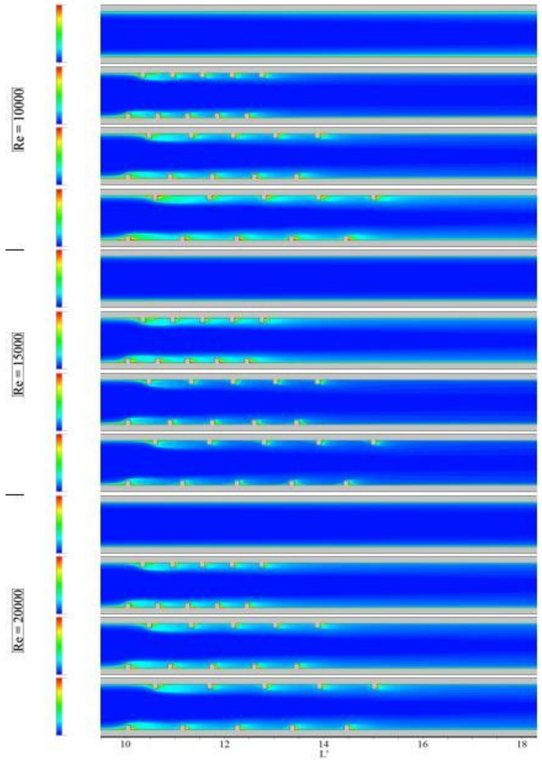

Figure 4. Time-averaged results of temperature distributions <T> for the ducts at Re = 10000, 15000 and 20000.

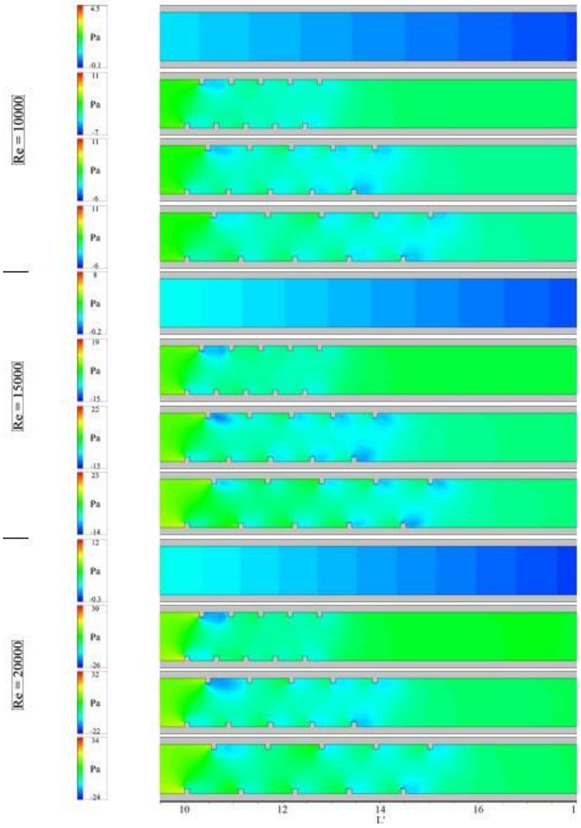

Figure 5. Time-averaged results of pressure distributions <P> for the ducts at Re = 10000, 15000 and 20000.

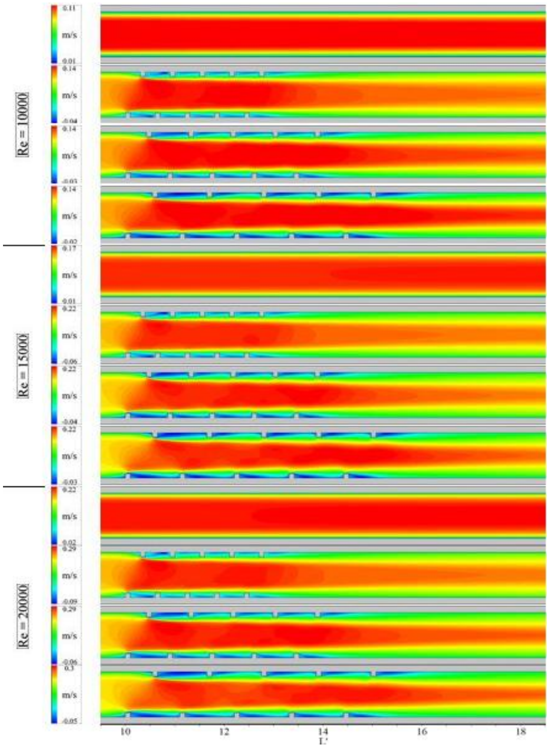

Figure 6. Time-averaged results of streamwise velocity components <u> for the ducts at Re = 10000, 15000 and 20000.

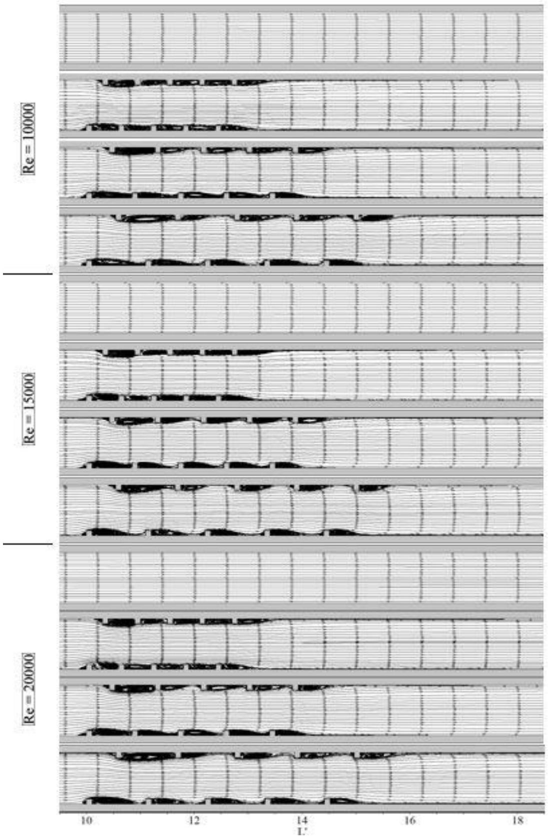

Figure 7. Time-averaged results of streamline patterns <Ψ> for the ducts at Re = 10000, 15000 and 20000.

Time-averaged results of mean Nusselt number values for the ribbed plates have been normalized with the values of Nusselt number of the smooth plates. These comparison charts have been presented in Figure 8 for all cases.

With respect to these graphics, Nusselt numbers have been increased by mounting the ribs on the plates. By extending the distance between two successive ribs, mean Nusselt numbers have also been increased. However, the rib effect on Nusselt number values is much more as clearly seen for Re = 10000. This effect has gradually been decreased for increasing Reynolds numbers.

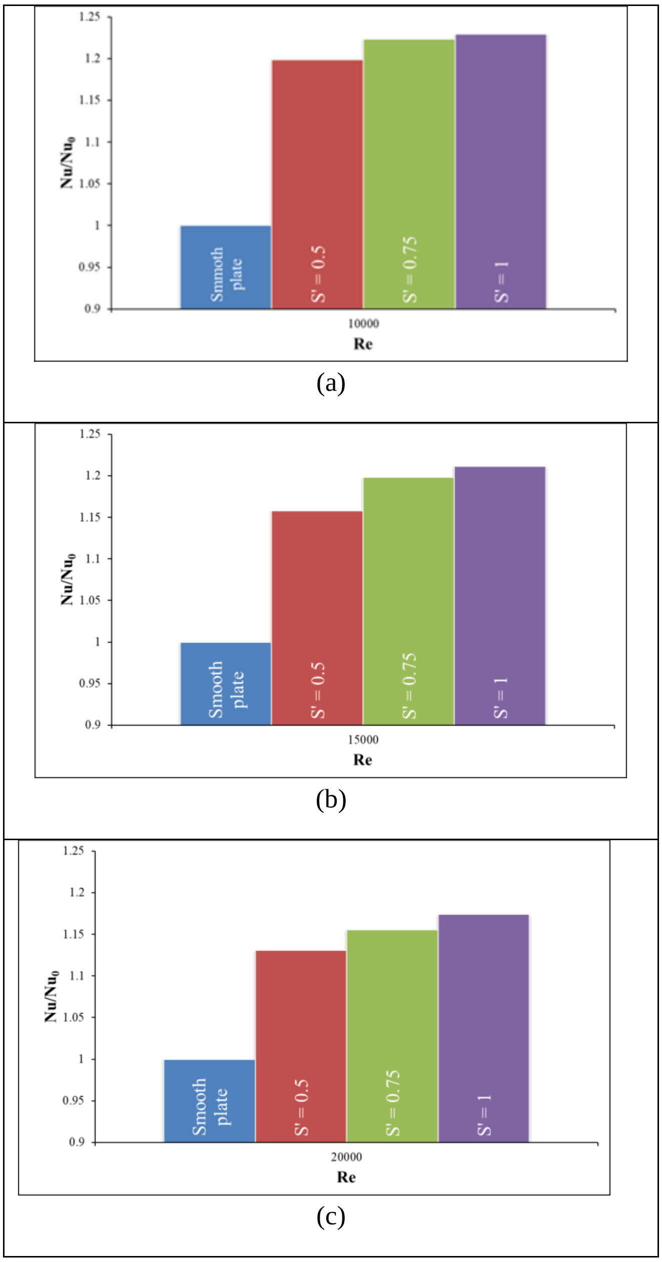

Figure 8. Time-averaged and normalized results of mean Nusselt number values for (a) Re = 10000, (b) 15000 and (c) 20000.

4. Conclusions

Heat transfer and turbulent flow characteristics between the plates have been numerically examined by considering the influence of the square cross-sectional ribs at $10000 \leq Re \leq 20000$ for the staggered arrangement in the present study. For the constant streamwise rib width of $w' = 0.1$, the dimensionless spacing have been varied as $0.5 \leq S' \leq 1$, respectively. All concluding remarks have been given by the following statements:

- For the smooth plates, heat transfer has only been enhanced owing to the increment of Reynolds number. For this reason, the heat transfer coefficient between the fluid and the plates has been increased.
- For the ribbed plates, more turbulent flow structure has been observed as compared to that of the case including no rib. This result is expressed by the deformation of hydrodynamic and thermal boundary layers because of the ribs on the plates.
- Increasing the rib spacing and Reynolds number has enhanced Nusselt number.
- Pressure loss for the case of smooth plate was less as expected for all Reynolds numbers. In case of the ribbed models, there are gradual drop pressure values along the channel. However, pressure loss values have increased because of increasing Reynolds number. In the meantime, placing the ribs on the plates also triggers the pressure drop.
- For most of the cases; the regions where the maximum values obtained in were the sinks bounded by the first two ribs and the upper side of the centerline. However, the margin between the ribs has almost no effect on the streamwise velocity components.
- As observed, heat transfer has also been augmented by extending the distance between two successive ribs since fluid easily penetrates to the sink between them for the production of recirculation regions.
- Average Nusselt numbers have been enhanced by the ribs on the plates. It has also been done by enlarging the gap between the ribs. However, the rib effect on these values is much more as evidently observed at $Re = 10000$. This effect has gradually been decreased for increasing Reynolds numbers.

Acknowledgements

The authors would like to acknowledge the funding of Academic Staff Training Program (OYP) for Project No. of 2018-OYP-046.

References

[1] Sundén B., 2011. Convective Heat Transfer and Fluid Flow Physics in Some Ribbed Ducts Using Liquid Crystal Thermography and PIV Measuring Techniques. Heat and Mass Transfer, **47**(8), pp.899–910.

[2] Alfarawi S., Abdel-Moneim S., Bodalal A., 2017. Experimental İnvestigations of Heat Transfer Enhancement From Rectangular Duct Roughened by Hybrid Ribs. International Journal of Thermal Sciences, **118**, pp.123–138.

[3] Tiggelbeck S., Mitra N.K., Fiebig M., 1993. Experimental İnvestigations of Heat Transfer Enhancement and Flow Losses in A Channel with Double Rows of Longitudinal Vortex Generators. International Journal of Heat and Mass Transfer, **36**(9), pp.2327–2337.

[4] Abdollahi A., Shams M., 2015. Optimization of Shape and Angle of Attack of Winglet Vortex Generator in A Rectangular Channel for Heat Transfer Enhancement. Applied Thermal Engineering, **81**, pp.376–387.

[5] Sripattanapipat S., Promvonge P., 2009. Numerical Analysis of Laminar Heat Transfer in A Channel with Diamond-Shaped Baffles. International Communications in Heat and Mass Transfer, **36**(1), pp.32–38.

[6] Manca O., Nardini S., Ricci D., 2011. Numerical Analysis of Water Forced Convection in Channels with Differently Shaped Transverse Ribs. Journal of Applied Mathematics 2011, 323485.

[7] Ahmed M., Yusoff M., Shuaib N., 2013. Effects of Geometrical Parameters on The Flow and Heat Transfer Characteristics in Trapezoidal-Corrugated Channel Using Nanofluid. International Communications in Heat and Mass Transfer, **42**, pp.69–74.

[8] Aslan E., Taymaz I., Islamoglu Y., 2016. Finite Volume Simulation for Convective Heat Transfer in Wavy Channels. Heat and Mass Transfer, **52**(3), pp.483–497.

[9] Moon M.A., Park M.J., Kim K.Y., 2014. Evaluation of Heat Transfer Performances of Various Rib Shapes. International Journal of Heat and Mass Transfer, **71**, pp.275–284.

[10] Kaewkohkiat Y., Promvonge P., Eiamsa-Ard S., 2017. Turbulent Periodic Flow and Heat Transfer in A Rectangular Channel with Detached V-Baffles. Journal of Engineering Thermophysics, **26**(4), pp.542–552.

[11] Patankar S., Liu C., Sparrow E., 1977. Fully Developed Flow and Heat Transfer in Ducts Having Streamwise-Periodic Variations of Cross-Sectional Area. Journal of Heat Transfer, **99**(2), pp.180–186.

[12] Liu H., Wang J., 2011. Numerical Investigation on Synthetical Performances of Fluid Flow and Heat Transfer of Semiattached Rib-Channels. International Journal of Heat and Mass Transfer, **54**(1-3), pp.575–583.

[13] Wongcharee K., Changcharoen W., Eiamsa-Ard S., 2011. Numerical Investigation of Flow Friction and Heat Transfer in A Channel With Various Shaped Ribs Mounted on Two Opposite Ribbed Walls. International Journal of Chemical Reactor Engineering, **9**(1), A26.

[14] Desrues T., Marty P., Fourmigué J., 2012. Numerical Prediction of Heat Transfer and Pressure Drop in Three-Dimensional Channels with Alternated Opposed Ribs. Applied Thermal Engineering, **45–46**, pp.52–63.

[15] Xie G., Li S., Zhang W., Sundén B., 2013. Computational Fluid Dynamics Modeling Flow Field and Side-Wall Heat Transfer in Rectangular Rib-Roughened Passages. Journal of Energy Resources Technology, **135**, 042001.

[16] Marocco L., Franco A., 2017, Direct Numerical Simulation and RANS Comparison of Turbulent Convective Heat Transfer in A Staggered Ribbed Channel with High Blockage. Journal of Heat Transfer, **139**(2), 021701.

[17] Promvonge P., Thianpong C., 2008. Thermal Performance Assessment of Turbulent Channel Flows over Different Shaped Ribs. International Communications in Heat and Mass Transfer, **35**(10), pp.1327–1334.

[18] Skullong S., Thianpong C., Promvonge P., 2015. Effects of Rib Size and Arrangement on Forced Convective Heat Transfer in A Solar Air Heater Channel. Heat and Mass Transfer, **51**(10), pp.1475–1485.

[19] Vanaki S.M., Mohammed H., 2015. Numerical study of nanofluid forced convection flow in channels using different shaped transverse ribs. International Communications in Heat and Mass Transfer, **67**, pp.176–188.

[20] Yang W., Xue S., He Y., Li W., 2017. Experimental Study On The Heat Transfer Characteristics of High Blockage Ribs Channel. Experimental Thermal and Fluid Science **83**, pp.248–259.

[21] Cengel Y.A. and Cimbala J.M., 2006. Fluid Mechanics Fundamentals and Applications, International Edition, McGraw Hill Publication, 185201.

[22] Matsubara K., Ohta H., Miura T., 2016. Entrance Region Heat Transfer in A Channel with A Ribbed Wall. Journal of Heat Transfer **138**(12), 122001.

[23] Anonymous, 2009. ANSYS-Fluent 12.0 Theory Guide, ANSYS Inc., USA.

[24] Yemenici O., Umur H., 2016. Experimental Aspect of Heat Transfer Enhancement over Various Flow Surfaces. Heat Transfer Engineering **37**(5), pp.435–442

Koc. J. Sci. Eng., 3(2): (2020) 41-45 https://doi.org/10.34088/kojose.804138

Kocaeli University

Kocaeli Journal of Science and Engineering

http://dergipark.org.tr/kojose

Experimental and Numerical Investigation of Crack Propagation in Spherical Porous Cylindrical Specimen under Mixed Mode Loading

Sedat İRİÇ [1,*]

[1] *Department of Mechanical Engineering, Sakarya University, Sakarya, 54187, Turkey,* ***ORCID:*** *0000-0001-8477-7906*

Article Info

Research paper

Received : October 02, 2020
Accepted : October 22, 2020

Keywords

Crack Propagation
Finite Element Simulation
Fracture Mechanics
Fracture Toughness
Stress Intensity Factor

Abstract

In this study, mixed mode I/III fatigue crack propagation is examined experimentally and numerically by using spherical porous cylindrical specimen. The crack propagation path, profiles of crack front, the differences of stress intensity factors (SIF) and equivalent SIF were computed by ANSYS, FCPAS and SOLIDWORKS softwares and compared with experimental data. Modeling, meshing and problem solving were performed using ANSYS, and the resulting SIF and equivalent SIF along the crack front were calculated using FCPAS. Two digital cameras were used to observing the crack growth path and fractured surfaces on specimen under mixed mode loading, and the obtained images were converted into 3D CAD data by using SOLIDWORKS software. It was found that good agreements were achieved between the results of the experiment and simulation considering both evolving the crack propagation paths and crack front.

1. Introduction

The applications of fracture mechanics have mainly focused on the prediction of the fatigue crack propagation and life of defective structures under mode I loading condition. But in industry, many service failures occur due to the crack is not perpendicular to the loading direction (mode I) or the structure is subjected to multiaxial (mixed mode) loadings. Under such mixed mode (mode I/III) loading conditions, out of plane (Mode III) loading can accelerate crack growth, and the crack may deviate from the original crack path. Thus, thorough understanding and knowledge of mechanisms driving mixed mode fracture and crack growth conditions are necessary for accurate assessment of such conditions computationally and experimentally. Linear elastic fracture mechanics (LEFM) approach has been widely used in analyzing the fatigue crack behavior where elastic stress-strain field in the vicinity of crack front is usually evaluated by calculating the SIF [1]. To investigate the SIF under mixed mode I/III loading conditions, some studies were performed experimentally and numerically. Yang et al. studied prediction of shape change for fatigue crack and validated by comparing the solution with other simulation solutions and experimental data [2]. Lin et al. examined the fatigue growth of surface, internal and multiple cracks in both notched and unnotched round bars subjected to remote tension or bending loads [3].Van et al. investigated the problem of crack propagation behaviour under tensile or bending fatigue loads. Comparisons were made with analytical, experimental and numerical results available in the literature [4]. Chaves et al. tested specimens with circular holes of various diameters under tension, torsion and in-phase biaxial loading [5]. Fatemi et al. investigated fatigue crack growth behaviour of tubular aluminium specimens with a circular hole under axial and torsional loadings [6]. Liu proposed various criteria for the calculation of effective mixed-mode SIF [7]. Schollmann et al., Sih et al. and Pook have developed three-dimensional (3D) criteria for the prediction of crack propagation, crack front profile and equivalent SIF [8-10]. Demir et al. have proposed a mixed mode I/II/III fracture criterion using both numerical and experimental analyses results [11]. Erdogan et al. have proposed the maximum tangential stress criterion [12]. Kurt et al. have made several 3D mixed mode fatigue crack propagation simulation using FCPAS software [13]. In this paper,

---

[*] Corresponding Author: siric@sakarya.edu.tr

numerical and experimental analyses were performed using spherical porous cylindrical specimen made of Al 7075-T651 to compare crack paths under tensile and torsion loadings.

2. Experimental Method

Test specimen used in this investigation was prepared from aluminum alloy 7075-T651 with 30 mm diameter. The mechanical properties of the alloy and the constants of the Paris equation in Eq. (1) for this material are listed in Table 1. In Eq. (1), E is the Young's modulus, σ_y is the yield tensile strength, C and m are the Paris constants. The Paris constants and fracture toughness (K_{IC}) of the materials were determined using standard notched and pre-cracked specimens [14-15].

Table 1. Main mechanical properties of Aluminum alloy 7075-651 [11].

E (GPa)	σ_y (MPa)	ν	K_{IC} (MPa√m)	C ($x10^{-7}$)	m
70	500	0.33	29.6	2.28	3.11

$$\frac{da}{dN} = C\Delta K_{eq}^{m} \tag{1}$$

The specimen geometry and test section dimensions are shown in Figure 1. A ball nose end mill cutter was used to prepare a spherical porous on one side of the specimen.

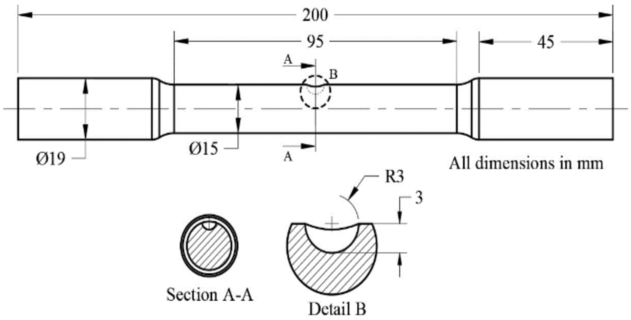

Figure 1. Details of the specimen geometry.

The axial/torsional test system (MTS 809) was used for mixed mode fatigue crack propagation testing of the specimen shown in Figure 2(a). The system was equipped with axial–torsional load cell with an axial capacity of 100 kN and torsional capacity of 1100 Nm. Before preparing the test setup, a finite element analysis (FEA) was performed to find maximum stress zone. Two independent 800x usb digital microscope cameras were used for the monitoring of the crack shown in Figure 2(c). Red color shows the maximum stress zone where are possible cracks initiation locations. The cameras were positioned to observe these area. This system has enabled simultaneous observation of two sides of the specimen during the fatigue test.

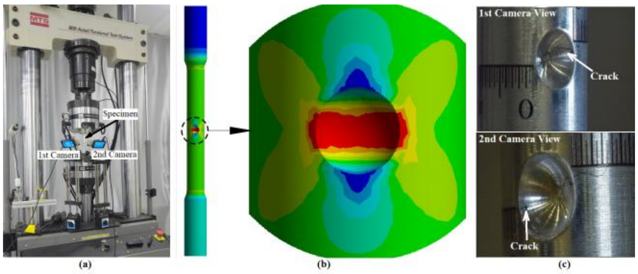

Figure 2. (a) Test setup (b) Maximum stress zone (c) Views of cameras.

The fatigue pre-crack was done at a maximum tensile load of 50 kN and the stress ratio R = 0.1. The test was stopped, when the surface crack length (a) observed with cameras was approximately equal to 1 mm (Figure 3(c)). Digital image observations of the specimen fractured surfaces were carried out in order to find the geometry of the pre-crack front shown in Figure 2(a-b). Obtained images were converted to 2D curve using curve fitting tool that is inside the SOLIDWORKS software. The blue dashed curve shown in Figure 2(c) was used to define the front of the crack for the fatigue crack propagation simulation under mixed-mode loading.

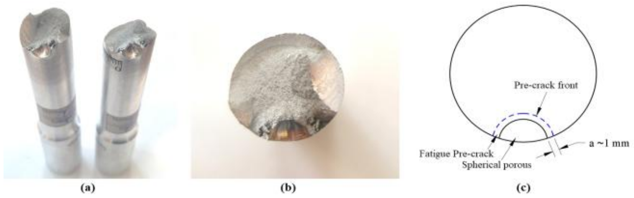

Figure 3. (a) Perspective view (b) Top view (c) Schematic representation of the pre-cracked section.

3. Numerical Modeling and Analysis

ANSYS, SOLIDWORKS and FCPAS software were used for modeling and analyzing the mixed mode fatigue crack propagation. The process steps of the analysis procedure are shown in Figure 4.

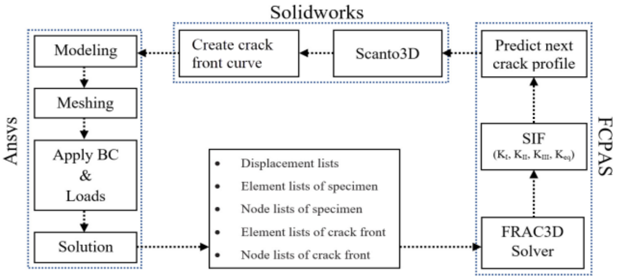

Figure 4. A detailed scheme of a fatigue crack propagation analysis.

The finite element model of the specimen was modeled as shown in Figure 1, and applied 40 kN tension and 150 Nm torsion loadings similar to the test conditions. Hexahedral enriched elements showed in red colour and transition elements showed in blue colour were used along and near the crack front, while remaining volumes are meshed using tetrahedral elements shown in Figure 5.

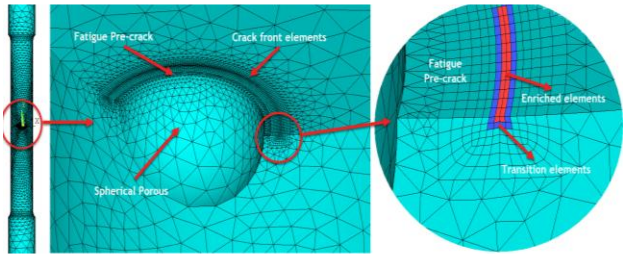

Figure 5. Detailed views of FEM model.

The finite element method (FEM) model was used to calculate some inputs for FCPAS as shown in Figure 4. FCPAS software was used to compute the SIFs along the crack tip under mixed mode loading using FRAC3D solver. The solver can compute SIFs using enriched crack front elements which do not need special mesh around the crack front [16-17]. The predicted crack propagation directions were examined by maximum tangential stress (MTS) criterion using calculated SIF. In Figure 6, variations of SIFs throughout the crack tip obtained from each growth step using FCPAS were presented. The SIF was shown a good agreement with Citarella's results.

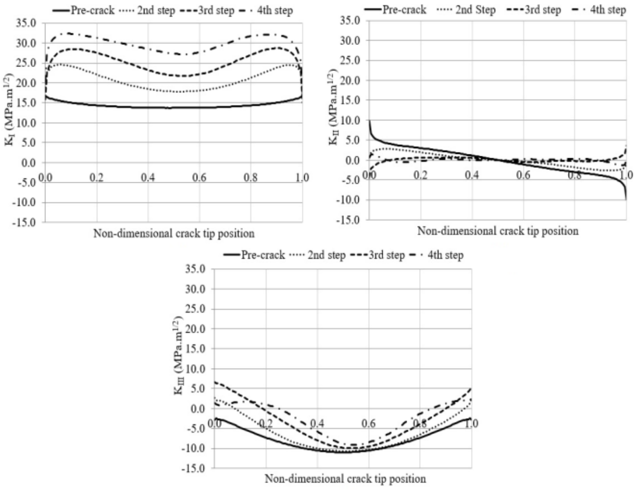

Figure 6. Distribution of K_I, K_{II} and K_{III} values for each step throughout the crack front.

The equivalent SIF was calculated using different criteria defined in FCPAS to compare results. When the stress intensity factor reaches the K_{IC} value, unstable fracture occurs. Fatigue crack propagation equation of Paris-Erdogan (Eq. (1)) was used for prediction of nodal crack propagation steps using the calculated equivalent SIF. The generated curve by FCPAS was converted to an elliptical and smooth form using SOLIDWORKS software, and then the curve was added to FEM model for crack propogation. This process was repeated until the equivalent SIF was reached to the fracture toughness (K_{IC}) of the material. The variation of SIF values (K_I, K_{II} and K_{III}) of the 1st step (pre-crack) and 4th step were shown in Figure 7 (a-b). The Richard et. al. 3D criteria were used to calculate the equivalent SIF by FCPAS. The calculated equivalent SIF values of 4th step was 30.2, 29.9, 30.7 and 33.5 MPa.m$^{1/2}$, respectively. At the 4th step, the equivalent SIF has reached the fracture toughness of the material as shown in Figure 8, therefore the numerical analysis process for fatigue crack propagation was completed.

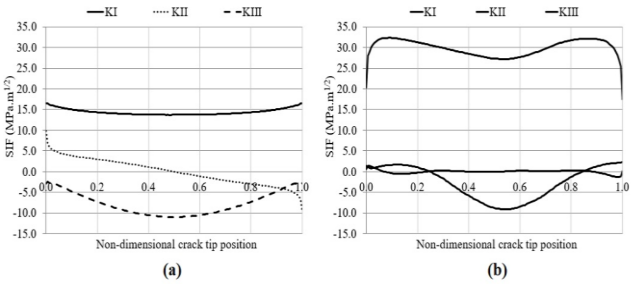

Figure 7. Variation of SIF values (a) 1st step (b) 4th step.

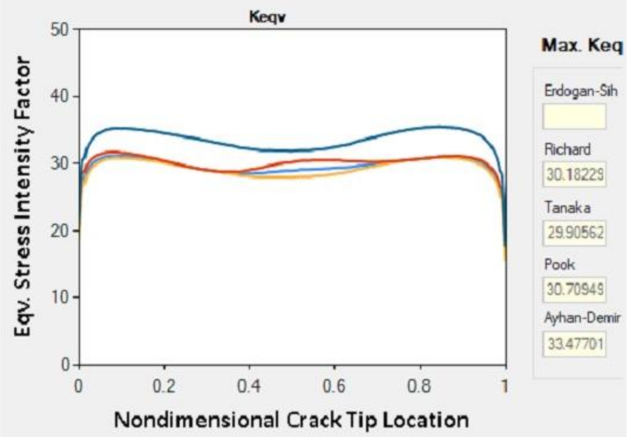

Figure 8. Variation of the calculated equivalent SIF values of 4th step by FCPAS.

4. Results and Discussion

Digital image examination of the specimen fracture surfaces were carried out in order to find the beginning of the stable and unstable crack growth zones as shown in Figure 9 (c). Using the examination in Figure 9 (a-b), the stable and unstable crack growth paths were also determined as shown in Figure 9(d).

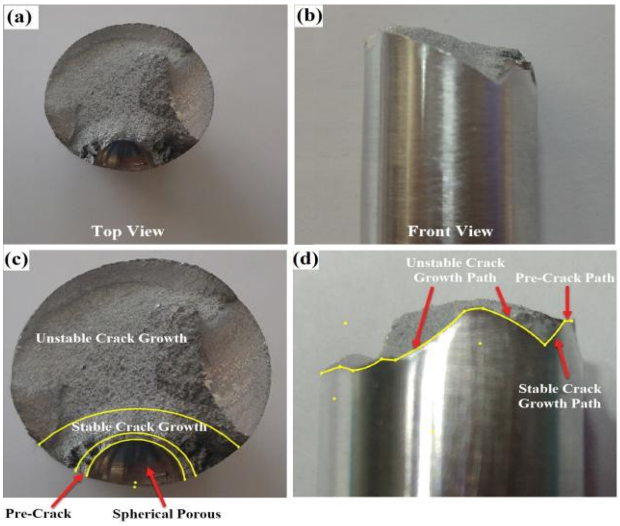

Figure 9. (a)Top, (b) Front views of the fractured specimen and (c) Zones of crack growth (d) Crack growth path.

In Figure 10, both the experimental and numerical images were overlapped to compare results. The dashed yellow line indicates the predicted the ith crack front. The simulation began with the pre-crack front determined by digital image and propagated with the calculated next crack front by FCPAS, until equivalent SIF was reached the fracture toughness. The calculated equivalent SIF for the 4th crack front was equal to the fracture toughness of the material shown in Figure 8. This means that unstable crack growth or fast fracture occurred. Very good agreements were obtained between the results of the simulation and experiment in terms of both evolving the crack growth paths and crack front as shown in Figure 10.

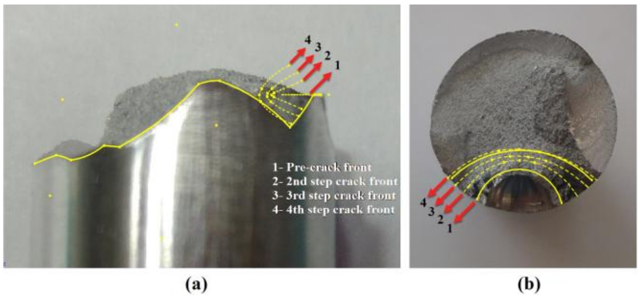

Figure 10. Overlapped views of the experimental and numerical simulation results (a) Front view, (b) Top view.

In Figure 10, the crack was propagated in-plane under Mode I loading during the pre-cracking, and then, propagation proceded out of the planes in three-dimensional space in mixed mode loading, as expected.

5. Conclusion

In this study, numerical and experimental studies for the surface crack propagation in cylindrical bar under combined cyclic tension-torsion loads were performed. When the above results are taken into consideration, this study has primarily yielded the following conclusions.

- Finite element modeling can be used accurately for study of mixed mode (I/III) fatigue crack propagation.

- The crack propagation direction can be predicted by using the MTS criterion for mixed mode I/III fatigue crack propagation.

- Throughout the crack front, KI values in the outer points are higher than those in the interior points at initial steps of crack propagation. However, with the further propagation of the crack, the differences decrease.

- KII values are close to zero and negligible in comparison with other modes.

- KIII values in outer points are higher than those in the interior points such as KI

- The all used criteria in FCPAS to calculate the equivalent stress intensity factor under mixed mode conditions are in very good agreement with the experimental measurements.

- There are no significant difference between the results of the simulation and experiment in terms of both evolving the crack growth paths and crack fronts.

- The presented methodology can be used to monitor the surface crack growth of the specific component at low frequency loading.

Acknowledgements

This work was supported by the Scientific and Technological Research Council of Turkey (TUBITAK), Project No: 217M690. I would like to thank Prof. Dr. Ali Osman Ayhan for allowing me to use the FCPAS software and also Strategic Products Research and Development Center (SARGEM) for the use of the facilities.

References

[1] Chandra D., Purbolaksono J., Nukman Y., 2018. Surface Crack Growth in A Solid Cylinder Under Combined Cyclic Bending-Torsion Loading. ARPN Journal of Engineering and Applied Sciences, **13**(3), pp. 1033-1041.

[2] Yang Y., Chu S., Chen H., 2019. Prediction of Shape Change for Fatigue Crack in a Round Bar Using Three-Parameter Growth Circles. Applied Sciences, **9**(9), p. 1751, doi:10.3390/app9091751.

[3] Lin X. B., Smith R. A., 1998. Fatigue Growth Simulation for Cracks in Notched and Unnotched Round Bars. International Journal of Mechanical Sciences, **40** (5), pp. 405-419.

[4] Van A. L., Royer J., 1993. Part-Circular Surface Cracks in Round Bars under Tension. Bending and Twisting, **61**(1), pp. 71-99.

[5] Chaves V., Beretta G., Balbín J. A., Navarro A., 2019. Fatigue Life and Crack Growth Direction in 7075-T6 Aluminium Alloy Specimens with a Circular Hole under Biaxial Loading. International Journal of Fatigue, **125**, pp. 222-236.

[6] Fatemi A., Gates N., Socie D. F., Phan N., 2014. Fatigue Crack Growth Behaviour of Tubular Aluminium Specimens with a Circular Hole under Axial and Torsion Loadings. Engineering Fracture Mechanics, **123**, pp. 137-147.

[7] Liu L., 2018. Modeling of Mixed-Mode Fatigue Crack Propagation, Tennessee, USA.

[8] Schollmann M., Richard H. A., Kullmer G., 2002. A New Criterion for the Prediction of Crack Development in Multiaxially Loaded Structures. International Journal of Fracture, **117**, pp. 129-141.

[9] Sih G. C., Barthelemy B. M., 1980. Mixed Mode Fatigue Crack Growth Predictions. Engineering Fracture Mechanics, **13**(3), pp. 439-451.

[10] Pook L., 1985. Comments on Fatigue Crack Growth under Mixed Modes I and III and Pure Mode III Loading. ASTM International, pp. 249-263, doi:10.1520/STP36227S.

[11] Demir O., Ayhan A. O., İriç S., 2019. A Novel Test System for Mixed Mode-I/II/III Fracture Tests – Part 2: Experiments and Criterion Development. Engineering Fracture Mechanics, doi:10.1016/j.engfracmech.2019.106671.

[12] Erdoğan F., Sih G. C., 1963. On the Crack Extension in Plates under Plane Loading and Transverse Shear. Journal of Basic Engineering, **85**(4), pp. 519-525.

[13] Kurt E., Demir O., Ayhan A. O., 2019. Applications on Three-Dimensional Mixed Mode Fatigue Crack Propagation Using Fracture and Crack Propagation Analysis System (FCPAS). Procedia Structural Integrity, **21**, pp. 32-30.

[14] Altuncu E., İriç S., 2017. Evaluation of Fracture Toughness of Thermal Sprayed and Hard Chrome Coated Aluminium-Zinc Alloy. Acta Physica Polonica A, **132**(3), pp. 926-929.

[15] İriç S., Ayhan A., 2017. Dependence of Fracture Toughness on Rolling Direction in Aluminium 7075 Alloys. Acta Physica Polonica A, **132**(3), pp. 892-895.

[16] Ayhan A. O., Nied H. F., 2002. Stress Intensity Factors for Three-Dimensional Surface Cracks Using Enriched Finite Elements. International Journal of Numerical Methods in Engineering, **54**, pp. 899-921.

[17] Ayhan A. O., Nied H. F. 1999. Finite Element Analysis of Interface Cracking in Semiconductor Packages. IEEE Transactions on Components and Packaging Technologies, **22**(4), pp. 503-511.

Koc. J. Sci. Eng., 3(2): (2020) 46-51 https://doi.org/10.34088/kojose.791802

Kocaeli University

Kocaeli Journal of Science and Engineering

http://dergipark.org.tr/kojose

Pyrolytic Degradation Behavior of Biomass Seeds: Sour Cherry and Peach Seed

Meltem KIZILCA ÇORUH [1,*], Hatice BAYRAKÇEKEN [2]

[1] *Department of Chemical Engineering, Atatürk University, Erzurum, 25240, Turkey,* ***ORCID:*** *0000-0001-8734-2502*
[2] *Department of Chemical Engineering, Atatürk University, Erzurum, 25240, Turkey,* ***ORCID:*** *0000-0003-2472-9974*

Article Info

Research paper

Received : *September 08, 2020*
Accepted : *October 05, 2020*

Keywords

Biomass
Flyn–Wall–Ozawa
Kissinger–Akahira–Sunose
Pyrolysis
Thermal Analysis

Abstract

Pyrolytic degradation behavior of peach and sour cherry seed were investigated by thermal analysis techniques such as thermogravimetric (TG) and derivative thermogravimetric (DTG). Pyrolysis study of peach and sour cherry seed, which are the sources of plant biomass, were carried out under air flowrate of 10 mL.min^{-1} and heating rates of 2.5,5,10 and 20 K min^{-1} in the temperature range of 298-1173 K by means of thermal analysis techniques. The activation energy and pre-exponential factor were determined with different methods as Kissinger–Akahira–Sunose (KAS) and Flyn–Wall–Ozawa (FWO). Although the FWO method gives higher values, it was observed that all activation energy values calculated by both methods are compatible with each other. In addition, as the amount of volatile matter increases, the decomposition becomes difficult due to the increase in mass transfer resistance and pressure, so it was determined that the activation energy of the peach seed is higher than the sour cherry seed.

1. Introduction

Nowadays, non-renewable (fossil) and renewable energy sources are used to meet the energy needs. The use of fossil fuels (petroleum, coal and natural gas) is quite common due to the fact that the costs of production, transportation and storage are cheap and easy [1]. Research on the availability and use of alternative renewable energy sources in the opposite of this negative situation of fossil resources and the obtained fuels has accelerated in recent years. One of them is biomass and has a great potential of biomass as a source in which various liquid hydrocarbons are obtained, especially for energy purposes [2]. One of the biggest advantages of biomass is that it is grown and consumed everywhere. In addition, biomass provides a clean solution to environmental problems and does not hinder the natural cycle of carbon. Compared to fossil fuels, environmental damage is very low. In particular, the combustion of biomass and CO_2/SO_2 emissions, known as greenhouse gases are so small that they do not affect the environment. The reason why biomass is preferred to fossil fuels in the following years; the contribution of biomass to the negative effects of global warming, which is expected to lead the world to a great disaster, will be very low. Biomass conversion processes for utilizing biomass can be separated into three basic categories: physical (milling, drying, filtration, extraction), thermochemical (direct combustion, gasification, pyrolysis, carbonization, liquefaction) and biochemical [3]. Pyrolysis is one of the most used thermochemical methods. Pyrolysis is the phenomenon the thermal decomposition by inert atmosphere or vacuum of organic material. As a result of the pyrolysis process, solid, liquid and gas products are obtained. The distribution and properties of the products obtained as a result of pyrolysis depend on both the process parameters and the type of biomass used. Temperature, heating rate, pressure, entraining gas in the environment, reactor geometry, retention time and the use of catalyst are the parameters affecting pyrolysis. Besides, particle size, moisture content, organic structure, inorganic content, porosity, constant carbon ratio, elemental composition of the raw materials affects the pyrolysis efficiency and product properties [4]. In addition to examining the parameters for design, optimization and control of biomass pyrolysis processes, it is of great importance to clarify the kinetic mechanism. The pyrolysis process is a solid state degradation and its kinetic

---

[*] Corresponding Author: mkizilca@atauni.edu.tr

parameters are determined by thermal analysis techniques such as thermogravimetric (TG) and derivative thermogravimetric (DTG). By means of the thermogravimetric analysis which can be done in isothermal or non-isothermal conditions, by using the weight loss data generated during the decomposition of solids, the separately kinetics and kinetic parameters can be determined for the degradation steps representing the total reaction kinetics or the degradation of the basic components [5]. Turkey has a strong agricultural potential. There are various agricultural residues, mainly food residues. In this study, two different biomass materials, sour cherry and peach, were used. According to the ecological conditions of many countries, the material should be selected considering that it should use the most suitable and economical agricultural and forest products as an alternative energy source. The reason for choosing these materials is because they have different structural and chemical properties and also have significant potential in renewable energy sources [6, 7]. In Turkey, the production of peach and sour cherry is 668.000 and 184.000 tons/year, respectively.

In this study, the pyrolytic degradation behaviors of peach and sour cherry seed were investigated by thermogravimetric analysis using different heating rates. Kinetic triplets which were activation energy, pre-exponential factor and pyrolysis mechanisms were calculated for different decomposition steps and total reaction with Kissinger–Akahira–Sunose (KAS) and Flyn–Wall–Ozawa (FWO) methods using data obtained from TG/DTG analysis.

2. Materials and Methods

2.1. Materials

Peach and sour cherry samples were purchased from a local supermarket in İstanbul, Turkey in February, 2019. Peach and sour cherry seeds were dried at room temperature and then ground to a 250 µm particle size for use in experiments. Structural and elemental analyses of the samples were performed before the thermoanalytical measurements. The chemical composition of peach and sour cherry seed has been previously reported [8, 9].

2.2. Thermal Analysis

The thermal analysis was carried out with NETZSCH STA 409 PC Luxx apparatus. Correction by reference data was done with an empty crucible at measurement conditions, identical to the sample measurement conditions. Approximately 10 mg of pattern was packaged in a platinum crucible. Experiments were taken with a pure nitrogen atmosphere flowrate of 10 mL min^{-1} under ambient conditions, over the temperature range of 298-1173 K, at a heating rate of 2, 5, 10 and 20 K min^{-1} and repeatable results were obtained. Platinum was used as the reference material. The experimental results obtained using the NETZSCH equipment were transformed to a MS Excel format file to draw TG-DTA curves and used to analyze the kinetics of dehydration.

2.3. Kinetic Analysis

In order to investigate the kinetics of the pyrolysis process, which is a solid phase decomposition process, the results obtained from thermogravimetric analysis was used. Active pyrolysis area determined by weight loss data obtained during biomass decomposition in thermogravimetric analysis and in order to determine kinetic parameters Kissinger–Akahira–Sunose (KAS) and Flyn–Wall–Ozawa (FWO) methods.

The Flyn-Wall-Ozowa (FWO) method Eq. (1), values of $1/T$ are plotted against log β for each conversion value (α). Activation energy (Ea) is calculated from the slope of parallel lines and pre-exponential factor (A) is determined from the intercept of the plot of Eq. (1) [5, 10, 11].

$$\ln(\beta) = \ln\left(\frac{AE_a}{g(\alpha)R}\right) - 5.331 - 1.052(\frac{E_a}{RT}) \tag{1}$$

The Kissinger–Akahira–Sunose (KAS) method Eq. (2), values of $1/T$ are plotted against the left side of equation for each α value. Activation energy (Ea) is calculated from the slope of parallel lines and pre-exponential factor (A) is determined from the intercept of the plot of Eq. (2) [5,11]:

$$\ln\left(\frac{\beta}{T^2}\right) = \ln\left(\frac{AE_a}{Rg(\alpha)}\right) - \frac{E_a}{RT} \tag{2}$$

where β is the heating rate, Ea is the activation energy, T is the obsolete temperature, A is the pre-exponential factor and R is the gas constant.

3. Result and Discussion

The TG-DTG curves corresponding to experiments carried out at four different heating rates (2, 5, 10, 15 and 20 K min^{-1}) in air atmosphere for the decomposition peach and sour cherry seed in Figure 1 and Figure 2, respectively. When the TGA diagrams given in Figures (1-2) were examined for each two samples, the different slopes were determined to have three weight loss zones. High substances of moisture and volatility.

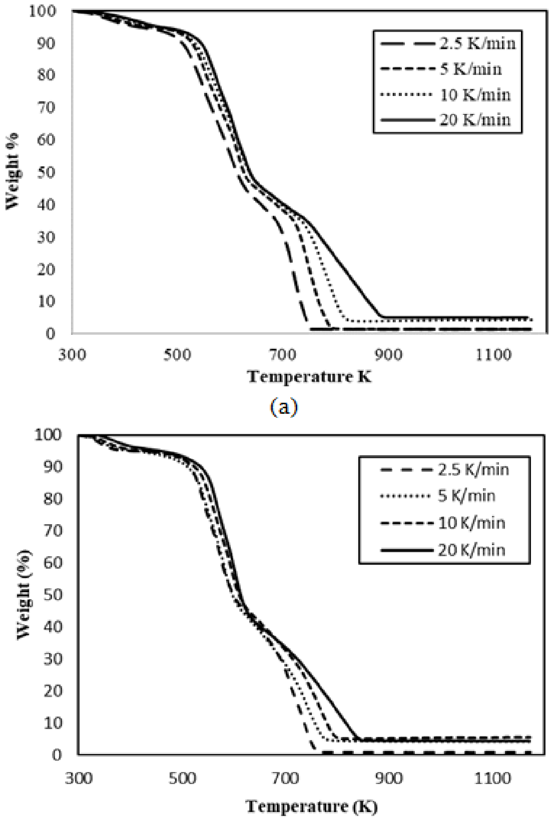

(a)

(b)

Figure 1. TG curves of a) sour cherry seed b) peach seed for different heating rates.

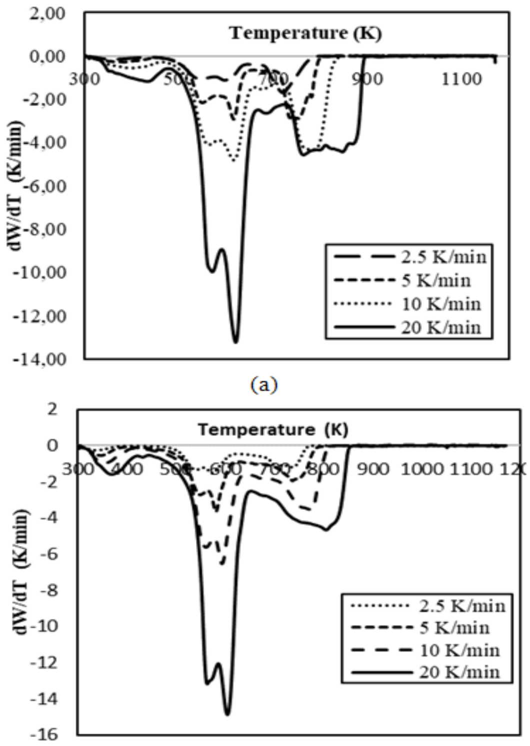

(a)

(b)

Figure 2. DTG curves of a) sour cherry seed b) peach seed for different heating rates.

The first region in the graphics is where it is separated from high humidity and volatile substances, and starting at 313 K and completed at 373 K, approximately the second region, where the weight loss on the TG curve is most marked, characterizes the degradation of hemicellulose and cellulose. This region starts at 513 K for seeds species and lasts up to 653 K. The third zone with slower loss of pain was identified as the thermal degradation zone of the lignin in the sample. The starting and ending temperature of the third zone were 653 K and 758 K respectively. Degradation continues in this region with gradually decreasing loss of mass. However, no significant change is observed in mass loss. After the mass loss becomes almost constant, only the carbon-rich solid product and ash remain from the lignocellulosic structure. Thus, when the temperature ranges of sour cherry and peach seed pyrolysis were examined, it was observed that the pyrolysis regions reflected the lignocellulosic structure of the biomass. E_a values were determined with the slope of the lnβ graph against 1000 / T (Figure 3 (a, b) for KAS method and Figure 4(a, b) for FWO method) between 0.1 and 0.9 values of fraction.

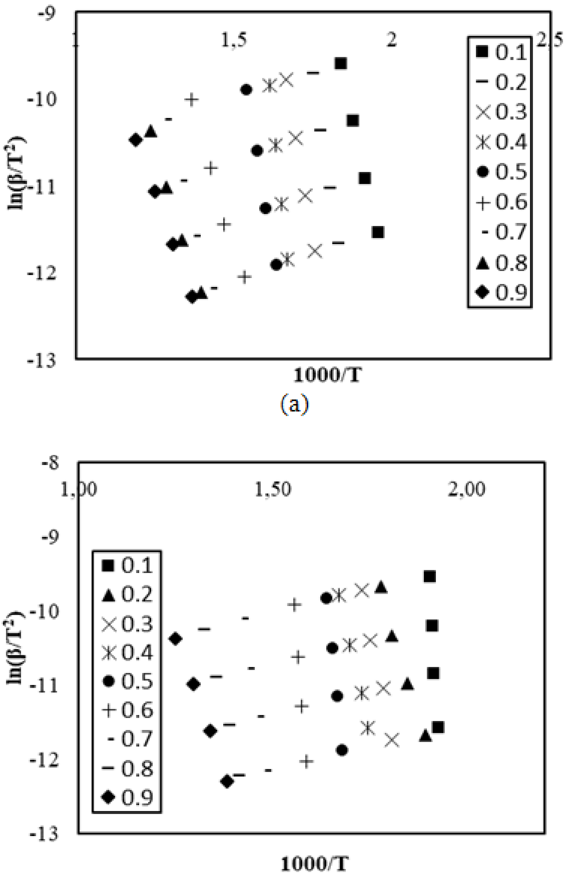

(a)

(b)

Figure 3. KAS method values for conversions from 0.1 to 0.9 ofthermal decomposition of a) sour cherry seed and b) peach seed.

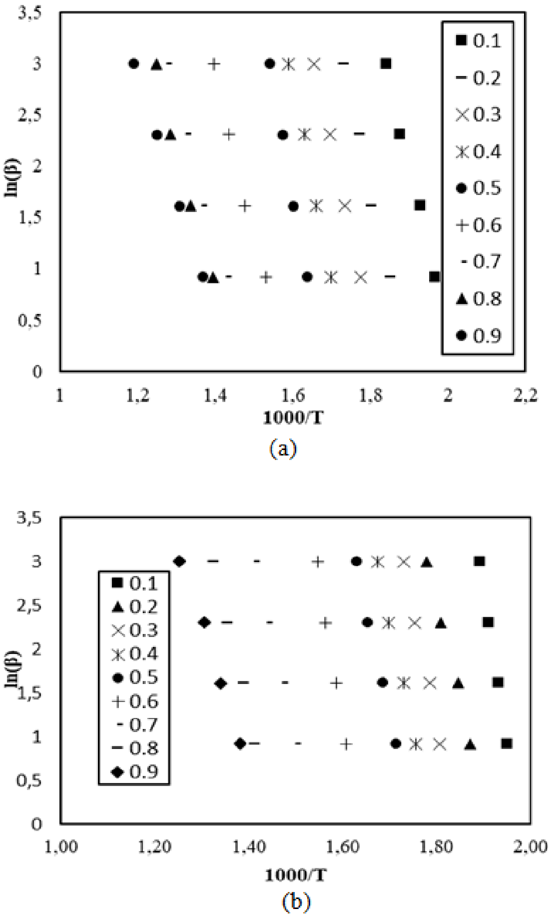

Figure 4. FWO method values for conversions from 0.1 to 0.9 of thermal decomposition of a) sour cherry seed and b) peach seed.

Activation energy, pre-exponential factor and regression coefficients calculated according to FWO and KAS methods (Eqs. (1-2)) are given in Table 1. It has been observed that there is a fluctuation in the activation energy by increasing the conversion fraction during the pyrolysis of peach and sour cherry seeds. The activation energy varies from 84.90 to 303.91 kJ / mol in the conversion range of 0.1-0.9. In the literature, there are many studies available showing the activation energy values for various biomass samples such as melon seed shell [12], chestnut shell [9], pistachio nutshell [13], tobacco waste [14], duckweed sample [15], and coffee husks [16]. The obtained activation energy is between 74-288 kJ mol-1. Thus, the activation energy values for sour cherry and peach seed calculated using the two models agree with the literature values. The change of the activation energy with the conversion fraction is related to the thermal degradation of the components of the biomass and is related to the thermal degradation of cellulose, hemicellulose and lignin. Increases and decreases in the activation energy indicate that the pyrolysis of the seeds is driven by multiple reaction mechanisms. When different kinetic methods were applied to the obtained data, the average activation energy values calculated by KAS and FWO methods were found as 125.77 and 135.59 kJ/mol for seed in Table 1 and 204.93 and 213.47 kJ/mol for peach seed in Table 2, respectively. The average of the exponential factor values tabulated in Tables (1-2) for sour cherry and peach seed were 27.77 and 44.34 for FWO and 13.03 and 34.12 for KAS methods, respectively, as calculated using Eqs. (1-2). The results showed that peach seed activation energy and pre-exponential values were higher than activation energy of sour cherry seed. The regression coefficients obtained from the kinetic analysis were found between 0.9746 and 0.9999. The fact that these numbers are close to 1 shows that the kinetic model used is a theoretical model equation that can successfully describe pyrolytic degradation.

Table 1. Activation energies and pre-exponential factor from KAS and FWO methods for the decomposition of sour cherry seed.

KAS				FWO		
α	E_a (kJ mol^{-1})	R^2	A (min^{-1})	E_a(kJ mol^{-1})	R^2	A (min^{-1})
0,1	17.93	0.9977	20.94	132.60	0.9958	32.31
0.2	19.01	0.9930	32.21	145.71	0.9919	33.35
0.3	17.56	0.9980	26.63	144.40	0.9999	31.76
0.4	19.52	0.9999	44.89	159.64	0.9965	33.56
0.5	175.25	0.9988	22.55	180.72	0.9994	36.47
0.6	104.41	0.9912	7.11	128.89	0.9945	24.60
0.7	114.80	0.9957	7.51	113.88	0.9932	20.44
0.8	99.41	0.9960	4.37	116.52	0.9907	20.40
0.9	84.90	0.9999	1.69	97.92	0.9999	17.02
Average	125.77		13.03	135.59		27.77

Table 2. Activation energies and pre-exponential factor from KAS and FWO methods for the decomposition of peach seed.

	KAS			FWO		
α	E_a (kJ mol^{-1})	R^2	A (min^{-1})	E_a(kJ mol^{-1})	R^2	A (min^{-1})
0,1	295.85	0.9746	57.81	303.91	0.9993	72.17
0.2	175.51	0.9903	21.58	182.96	0.9960	42.13
0.3	207.73	0.9919	33.46	215.13	0.9933	47.71
0.4	181.973	0.9952	29.04	208.33	0.9967	44.91
0.5	200.89	0.9991	72.45	205.41	0.9970	43.23
0.6	290.03	0.9816	44.04	286.50	0.9966	56.28
0.7	190.14	0.9956	22.20	194.70	0.9987	36.07
0.8	178.37	0.9931	18.18	189.41	0.9947	33.19
0.9	123.85	0.9987	8.34	223.29	0.9912	23.35
Average	204.93		34.12	213.47		44.34

4. Conclusions

Pyrolysis study of peach and sour cherry seed, which are the sources of plant biomass, are carried out at different heating rates by means of thermal analysis techniques (TG/DTG). In the TG curve of peach and sour cherry seed, thermal change was recorded in three regions, which are the separation of moisture and high volatile components, breaking of hemicellulose and cellulose and degradation of lignin at high temperature, depending on the temperature. Energy values calculated by KAS and FWO methods were found as 125.77 and 135. 59 kJ/mol for sour cherry seed and 204.93 and 213.47 kJ/mol for peach seed, respectively. The average activation energy values calculated by both methods are compatible with each other. The proximity of these values indicates that preferred kinetic models can successfully identify pyrolytic degradation.

References

[1] Özsina G., Eren Pütün A., 2019. TGA/MS/FT-IR Study for Kinetic Evaluation and Evolved Gas Analysis of a Biomass/PVC Co-pyrolysis Process. Energy Conversion and Management, **182**, pp.143–153.

[2] Demirbaş A., 2001. Biomass Resource Facilities and Biomass Conversion Processing for Fuels and Chemicals. Energy Conversion and Management, **182**, pp.143–153.

[3] Zhang L., Xu C., Champagne P., 2010. Overview of Recent Advances in Tthermo-chemical Conversion of Biomass. Energy Conversion and Management, **51**, pp. 969–982.

[4] Samolada M. C., Stoicos T., Vasalos I. A., 1990. An Investigation of the Factors Controlling the Pyrolysis Product Yield of Greek Wood Biomass in a Fluidized Bed. Journal of Analytical and Applied Pyrolysis, **18**, pp. 127-141.

[5] Kızılca M., Copur M., 2016. Investigation of the Thermal Decomposition Kinetics of Chalcopyrite Ore Concentrate Using Thermogravimetric Data. Chemical Engineering Communications, **203**, pp. 692-704.

[6] Özçimen D., Ersoy-Meriçboyu A., 2008. A Study on the Carbonization of Grapeseed and Chestnut Shell. Fuel Process Technol, **89**, pp. 1041-1046.

[7] Özçimen D., Ersoy-Meriçboyu A., 2010. Characterization of Bio Char and Bio-oil Samples Obtained from Carbonization of Various Biomass Materials. Renewable Energy, **35**, pp. 1319-1324.

[8] Luz Bengoechea M., Sancho Begon I., Estrella I., Gomez-Cordoves C., Hernandez M. T., 1997. Phenolic Composition of Industrially Manufactured Pure´es and Concentrates from Peach and Apple Fruits. Journal of Agricultural and Food Chemistry. **45**, 4071−4075.

[9] Özsin G., Eren Pütün A., 2018. Co-pyrolytic Behaviors of Biomass and Polystyrene: Kinetics, Thermodynamics and Evolved Gas Analysis, Korean J. Chem. Eng., **35**, pp. 428-437.

[10] Kantürk Figen A., Sarı Yılmaz M., Pişkin S., 2010. Structural Characterization and Dehydration Kinetics of Kırka Inderite Mineral: Application of Non-isothermal Models. Materials Characterization, **61**, pp. 640-647.

[11] Kızılca M., Copur M., 2017. Thermal Dehydration of Colemanite: Kinetics and Mechanism Determined Using the Master Plots Method. Canadian Metallurgical Quarterly, **56**, pp. 259–27.

[12] Ahmed A., Afolabi E. A., Garba M. U., Musa U., Alhassan A,. Ishaq I., 2019. Effect of Particle Size on Thermal Decomposition and Devolatilization Kinetics of Melon Seed Shell. Chemical Engineering Communications, **206**, pp. 1228–1240.

[13] Isıtan S., Ceylan S., Topcu Y., Hintz C., Tefft J., Chellappa T., Guo J., Goldfarb J. L., 2016. Product Quality Optimization in an Integrated Biorefinery: Conversion of Pistachio Nutshell Biomass to Biofuels and Activated Biochars via Pyrolysis. Energy Conversion and Management, **127**, pp. 576–588.

[14] Polat S., Apaydin-Varol E., Eren Pütün A., 2016. Thermal Decomposition Behavior of Tobacco Stem Part II: Kinetic Analysis. Energy Sources, Part A: Recovery, Utilization, and Environmental Effects, **38**, pp. 3073–3080.

[15] Liu H., Ahmad M. S., Alhumade H., Elkamel A., Sammak S., Shen B., 2020. A Hybrid Kinetic and Optimization Approach for Biomass Pyrolysis: The Hybrid Scheme of the Isoconversional Methods, DAEM, and a Parallel Reaction Mechanism. Energy Conversion and Management, **208**, 112531.

[16] Setter C., Silva F. T. M., Assis M. R., Ataíde C. H., Trugilho P. F., Oliveira, T. J. P.,, 2020. Slow Pyrolysis of Coffee Husk Briquettes: Characterization of the Solid and Liquid Fractions. Fuel, **261**, 116420.

Koc. J. Sci. Eng., 3(2): (2020) 52-58 https://doi.org/10.34088/kojose.770729

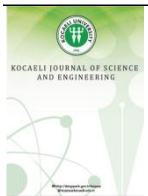

Kocaeli University

Kocaeli Journal of Science and Engineering

http://dergipark.org.tr/kojose

Size of Earthquakes

Mehveş Feyza Akkoyunlu [1, *]

[1]*Regional Earthquake-Tsunami Monitoring Center, Kandilli Observatory and Earthquake Research Institute, Istanbul, 34684, Turkey,*
ORCID: *0000-0002-4966-8218*

Article Info

Review paper

Received : *July 17, 2020*
Accepted : *October 25, 2020*

Keywords

Earthquakes,
Earthquake Size,
Intensity,
Magnitude,
Macroseismic Intensity Scale

Abstract

Earthquake size is one of the most fundamental source parameters used in seismic catalogs. A reliable measure of the "size" of an earthquake is essential for seismological, geological, engineering, and scientific research. The size of a seismic source is measured using two parameters; damage caused (intensity) and energy released (magnitude). Intensity describes the strength of a seismic event in terms of human recognition, affected region, damage to structures. Intensity scales are valuable not only for the pre-instrumental period for historical earthquakes but also for seismic risk analysis. The intensity scale is classified by macroseismic scales. Intensity depends on local geological conditions, distance from the source that make the objective estimates difficult. The concept of magnitude was introduced by Richter to provide an objective measure of earthquake size. The advent of seismic recording systems made it possible to determine the strength of a seismic event from instrumental data. The magnitude of an earthquake provides quick information on the strength of a seismic event for the public and are essential for cataloging. Changes in instrumentation and magnitude formulation resulted from the calculation of different magnitude scales. In order to obtain a non-saturating uniform magnitude scale, seismic moment magnitude (Mw) is developed based on source parameters.

1. Introduction

Macroseismic intensity scales represent the intensity of ground-motion in terms of human observation, damage to buildings, or other observed effects at a certain location. Felt reports and damage in an area are sources of intensity estimation of an earthquake. Macroseismic intensities are important for historical seismicity and assessment of seismic hazard risk studies. Intensity depends on many factors such as local geological conditions, distance, and depth of the earthquake. The energy released from a seismic source may be may be amplified or diminished by ground motion. Macroseismic intensity classifies the severity of earthquakes depending on damage at different locations and felt shaking records. These factors are affected by the quality of construction and the density of the population [1].

An instrumental scale was necessary to characterize the size of a seismic event based on instrumental records. According to Richter (1935) "In the course of a historical or statistical study of earthquakes in a given region, it is frequently desirable to have a scale for rating these shocks in terms of their original energy, independently of the effects which may be produced at any particular point of observation" [2].

The advent of seismic recording instruments led to quantifying the strength of a seismic event by the amplitude of the recorded signal. The magnitude concept was first proposed in the 1930s by Wadati in Japan and Richter in California. The magnitude of an event is a number that characterizes the relative size or amount of energy released by an event which is independent of the place of observation. Magnitudes are derived from ground motion amplitudes and periods or from signal duration obtained from instrumental records and source parameters of the earthquake including seismic waves.

---

[*] Corresponding Author: feyza.ocal@boun.edu.tr

2. Macroseismic Intensity Scales

The size of seismic sources is characterized by the macroseismic intensity scale before the advent of seismic recording instruments. The intensity or macroseismic intensity is an integer quantity that depends on earthquake distance, ground conditions, and strength of shaking. Intensities are defined in macroseismic scales.

The first studies took place in Italy at the end of the 18th century. The Ten-degree Rossi-Forel scale (1883) was the first scale to be used internationally. The first 12-degree scales were introduced by Sieberg, and Mercalli, Cancani and Sieberg (1912, 1923, 1932, MCS scale). The Modified Mercalli Scale (MM scale) was revised by Richter in 1956 (MM56 scale) and used in the USA. In Europe, MSK-scale is developed by Medvedev, Sponheuer, and Karnik (1964) was widely used. In 1988 MSK-scale is revised by European Seismological Commission and European Macroseismic Scale (EMS-98) is released in 1998 and widely adopted all over the world. Earthquake intensities in Japan contain 7–degree (later upgraded to 10-degree) by Japan Meteorological Agency (JMA). Macroseismic intensity is dependent on the local geological conditions, the distance from the source, quality of the construction and, density of the population.

The intensities generally decrease with distance from the source and are site-dependent. They represent the severity of ground-motion during a seismic event on the basis of observational effects of the region, human perception, and damage to buildings.

Intensity is a measure of the strength of the seismic source and a description of common observations of an earthquake. Instead of describing the effect of an earthquake-like “the event was felt by very few people indoors”, the shaking is shortly defined as “intensity 2”. Each intensity degree is expressed by a series of diagnostic that describes the effects of ground motion. Intensity data are mapped in contour lines for different degrees called isoseismals. The largest observed intensity is the epicentral intensity I_0 near to the epicenter or barycenter of the highest intensities. The most recent scales are the Modified Mercalli Scale (MMI) and European Macroseismic Scale (EMS-98) which are easily adaptable for the use to building stock anywhere in the world. In Table 1, MMI Scale of Stover and Coffman edited by Musson is shown as an example for the intensity scale [3].

Table 1. MMI Scale of 1993 (Stover and Coffman, after Wood and Neumann, edited by Musson).

I	Not or rarely felt under especially favourable circumstances. Under certain conditions, at and outside the boundary of the area in which a great shock is felt: sometimes birds, animals, reported uneasy or disturbed; sometimes dizziness or nausea experienced; sometimes trees, structures, liquids, and bodies of water may sway, doors may swing very slowly.
II	Felt by few sensitive, or by nervous persons indoors, especially on upper floors. Also, as in grade I, and often more noticeably: sometimes hanging objects may swing, especially when delicately suspended; sometimes trees, structures, liquids, bodies of water may sway; doors may swing very slowly; sometimes birds, animals reported uneasy or disturbed; sometimes dizziness or nausea experienced.
III	Usually rapid vibration motion felt indoors by several people. Sometimes not recognized to be an earthquake at first. Continuity estimated in some cases. Vibration occures due to the passing of light, or lightly loaded trucks, or heavy trucks some distance away. Hanging objects may swing slightly. Movements may be appreciable on upper levels of high structures. Rocked standing motor cars slightly.
IV	Felt by all. Many get frightened. Trees and bushes shake slightly. Buildings shake moderately to heavily. Walls creak loudly. Observers described the shaking as "strong." Few get awakened, especially light sleepers. No one is frightened, unless apprehensive from previous experience. Vibration happens due to the passing of heavy or heavily loaded trucks. Sensations like heavy body striking building or falling of heavy objects are seen inside. Rattling of dishes, windows, doors; glassware and crockery clink and clash. Hanging objects swung, in numerous instances. Liquids in open vessels disturb slightly. Standing motor cars rock noticeably.

Table 1. (Cont.) MMI Scale of 1993 (Stover and Coffman, after Wood and Neumann, edited by Musson).

V	Buildings tremble during the quake. Dishes, glassware break to some extent. Windows crack - in some cases, but not generally. Vases, small or unstable objects overturne in many instances. Hanging pictures fall. Doors, shutters, open, or close abruptly. Pendulum clocks stop, start or run fast, or slow. Small objects, furnishings, move the latter to a slight extent. Trees, bushes, shake moderately to strongly. People have difficulty in standing or walking. People feel moderately in moving vehicles.
VI	Damage is slight in poorly built buildings. Fall of plaster is seen in a small amount. The plaster layer cracks somewhat, especially fine cracks in chimneys in some instances. Dishes, glassware, in considerable quantity, also some windows break. Fall of knickknacks, books, pictures. Furniture overturne in many instances. Furnishings of moderately heavy kind move. Small bells ring - church, chapel, school, etc. The intensity can only be assessed as VI if damage to buildings is observed, unless many small objects fall from shelves or many glasses or dishes break.
VII	Damage neglected in buildings of good design and construction, from slight to moderate in well-built ordinary buildings, considerable in poorly built or badly designed buildings, adobe houses, old walls (especially where laid up without mortar), spires, etc. Chimneys get cracked to a considerable size, and walls to some extent. Fall of plaster in considerable to large amount, also some stucco. Numerous windows and some furniture break. Loosened brickwork and tiles shake down. Weak chimneys break at the roofline (sometimes roofs damaged). Fall of cornices from towers and high buildings. Bricks and stones dislodge.

Table 1. (Cont.) MMI Scale of 1993 (Stover and Coffman, after Wood and Neumann, edited by Musson).

VIII	Slight damage in structures (bricked) built especially to withstand earthquakes. Partial collapse considerable in ordinary substantial buildings. Wooden houses rack, tumble down in some cases, panel walls in frame structures thrown out, and decayed pilings break off. Fall of walls. Solid stone walls crack and break seriously. Chimneys, columns, monuments, also factory stacks, towers fall or twist. Very heavy furniture move or overturn conspicuously. Trees shake strongly - branches, trunks, break off, especially palm trees.
IX	Damage considerable in (masonry) structures built especially to withstand earthquakes: break of some plumb wood-frame houses built especially to withstand earthquakes; great extent damage in substantial (masonry) buildings, some collapse in large part; or wholly shifted frame buildings off foundations and racked frames.
X	Damage serious to dams, dykes, embankments. Severe to well-built wooden structures and bridges, some destroyed. Dangerous cracks develop in excellent brick walls. Most masonry and frame structures, as well as their foundations, destroy.
XI	Damage severe to wood-frame structures, especially near shock centres. Great to dams, dikes, embankments often for long distances. Few, if any (masonry) structures remained standing. Destroyed large well-built bridges by the wrecking of supporting piers, or pillars. Less affected yielding wooden bridges.
XII	Total damage - practically all parts of construction wholly damage or destroy.

The simplified short form of EMS-98 (abstracted) [3] is shown in Table 2.

Table 2. Short Description of EMS-98 (Abstracted).

I	**Not felt**	Not felt
II	**Scarcely felt**	Felt only by very few individuals at rest in their homes.
III	**Weak**	Felt indoors by a few people. People at rest feel a swaying or light trembling.
IV	**Largely observed**	Felt by many people indoors, but by very few outdoors. A few people are awakened. Windows, doors and dishes rattle.
V	**Strong**	Felt by most indoors, by few outdoors. Many sleeping people wake up. A few are frightened. Buildings tremble in the meantime. Hanging objects swing considerably. Small objects are shifted. Doors and windows swing open or shut.
VI	**Slightly damaging**	Many people are frightened and run outdoors. Some objects fall. Some houses suffer slight non-structural damage like hair-line cracks and fall of small pieces of plaster.
VII	**Damaging**	Most people are frightened and run outdoors. Furniture is shifted and objects fall from shelves in large numbers. Many well-built ordinary buildings suffer moderate damage: small cracks in walls, fall of plaster, parts of chimneys fall down; older buildings may show large cracks in walls and failure of fill-in walls
VIII	**Heavily damaging**	Many people find it difficult to stand. Many houses have large cracks in walls. A few well-built ordinary buildings show serious failure of walls, while weak and older ones may collapse.
IX	**Destructive**	General panic. Many weak constructions collapse. Even well-built ordinary buildings show very heavy damage: serious failure of walls and partial structural failure.
X	**Very destructive**	Many ordinary well-built buildings collapse.
XI	**Devastating**	Most ordinary well-built buildings collapse; even some with good earthquake resistant design are destroyed.
XII	**Completely devastating**	Almost all buildings are destroyed.

Table 2. (Cont.) Short Description of EMS-98 (Abstracted).

Macroseismic data is gathered by several methods. The main source of the data is the collection of the questionnaires. The questionnaires are important to collect data from a large number of observations. A web-based program called “Did you Feel It?” by USGS [4] is an international questionnaire. Field studies should be held to collect information on earthquake damages of the buildings. [5]. In Figure 1, the intensity map of 24 January 2020 Sivrice-Elazığ earthquake is given as an example [6].

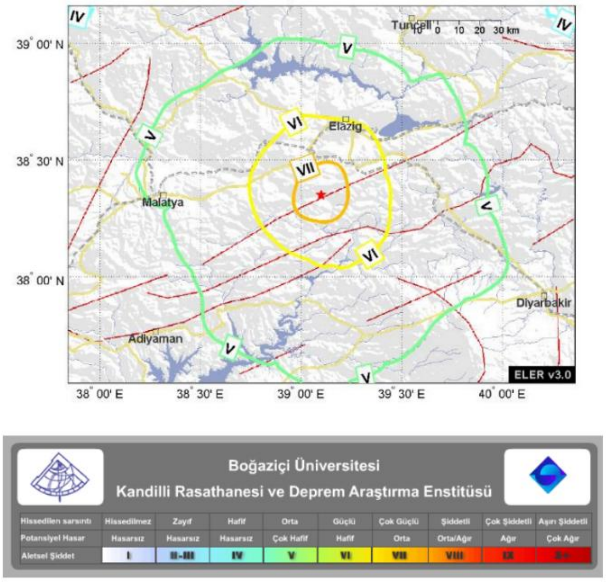

Hissedilen sarsıntı	Hissedilmez	Zayıf	Hafif	Orta	Güçlü	Çok Güçlü	Şiddetli	Çok Şiddetli	Aşırı Şiddetli
Potansiyel Hasar	Hasarsız	Hasarsız	Hasarsız	Çok Hafif	Hafif	Orta	Orta/Ağır	Ağır	Çok Ağır
Aletsel Şiddet	I	II-III	IV	V	VI	VII	VIII	IX	X+

Figure 1. Screenshot from the KOERI website, showing a macroseismic display of 24 January 2020 Sivrice-Elazığ earthquake.

3. Earthquake Magnitude Scales

Earthquake magnitude is a parameter used in seismology to quantify the size of an earthquake based on the measurement of the maximum ground motion recorded by a seismograph. There is no scale limitation to magnitudes as in macroseismic intensity scales. Magnitudes are commonly derived from ground motion amplitudes and periods or from duration of seismic signals measured on instrumental records. The same earthquake might have different magnitude values on different scales. The magnitude scales above are dependent on a certain signal frequency.

The magnitude of an event is based on and corrected for the decay of amplitudes with epicenter distance and source depth.

Charles F. Richter (1935) introduced Richter magnitude [7] or local magnitude (M_L) and defined it as:

“*The magnitude of a shock is defined as the logarithm of the calculated maximum trace amplitude, expressed in microns, with which standard short-period torsion seismometer (T0=0.8, V=2.8000, h=0.8) would register that shock at the epicentral distance of 100 km).”*

Richter scale termed as ML and applicable local earthquakes are formulated as:

$$M_L = \log A_{max} - \log A_0\,(\Delta) \qquad (1)$$

where A_{max} is the seismogram amplitude measured on a Wood-Anderson record and the distance Δ to the source. Generally all magnitude scales are a form of

$$M = \log\left(\frac{A}{T}\right) + f(\Delta, h) + C_{source} + C_{receiver} \qquad (2)$$

where T is the period of the signal, $f(\Delta, h)$ is a correction for epicentral distance and hypocenter depth. Empirical correction values for the source region and the receiver site are added. In Richter’s formula, as all the seismographs were of the same type dependence on T was missing, maximum amplitude always had the same dominant period.

For global earthquake size calculations, the local magnitude scale is not practical. Gutenberg and Richter designed magnitude scales for global magnitude scales. Body-wave magnitude (m_b) is calculated by maximum ground-motion amplitude of P, PP, or S body waves, and defined as

$$m = \log\left(\frac{A}{T}\right) + Q(\Delta, h) \qquad (3)$$

where Q is an empirically determined distance and depth correction, depending on the phase used. If the body-wave magnitude is determined from P wave at a period of 1s, it is generally abbreviated as m_b. When determined from long-period instruments at periods between 5-15 seconds, it is noted as m_B.

Surface wave magnitude scale uses the maximum ground motion amplitude of surface wave at a period of 20s. In general, Rayleigh wave amplitude is used for the calculation of M_s. The formula for this surface-wave magnitude is defined as

$$M_S = \log A_{20s} + 1.66\, log\, \Delta + 2.0 \qquad (4)$$

As the size of the earthquake increases, the low-frequency part of its spectrum relative to the higher frequencies is stronger. This will cause magnitude saturation for large earthquakes. Seismic moment calculation was introduced by Kanamori [8] to provide a non-saturating magnitude scale for large earthquakes termed as moment magnitude (M_w) based on seismic moment (M_0). The seismic moment M_0 can be determined by seismic data, geodetic data or geological data [9].

Seismic moment can be found accurately from seismic data [9]. The seismic moment calculation constitutes the fault area, slip, and strength of the material which represents the physical measure of an earthquake. It can be obtained from amplitudes of seismic waves or from the field estimations of the slip and fault area of the earthquake. For a finite source with area of fault plane (S), on which the averaged slip is D (offset, in km) and μ (Gpa) is shear or the rigidity modulus of the material surrounding the fault, the M_0, scalar seismic moment is given as

$$M_0 = \mu DS \qquad (5)$$

In cgs units, the seismic moment is given in dyn cm and in SI units it is in Nm.

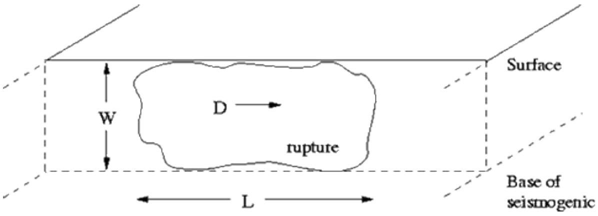

Figure 2. Diagram of an area of the fault rupture on earthquake area [10].

The moment magnitude (M_w) and seismic moment (M_0) relation is defined as by the following [9]. M_0 is a static parameter that does not represent dynamic properties of the source unless the use of scaling relations exist. M_0 or M_w can be used as a useful parameter for the earthquake damage effects [9].

$$M_w = \frac{log_{10} M_0}{1.5} - 6.07 \quad (M_0\ in\ Nm) \qquad (6)$$

Magnitude scales are affected by not only observational errors but also fault geometry, size and source depth of the earthquake. The magnitude scales determined at different periods represent different parts of the seismic source spectrum. Various magnitude scales [M_s, m_b, M_L, M_w) calculated for earthquake catalogues will be useful for research purposes [9]. As the range of period for different magnitude scale change, magnitude scales saturate differently. The relations between various magnitude scales are summarized in a graphical form representing the saturation of m_b, m_B, M_L, M_s by [11-12] in Figure 2. and Figure 3.

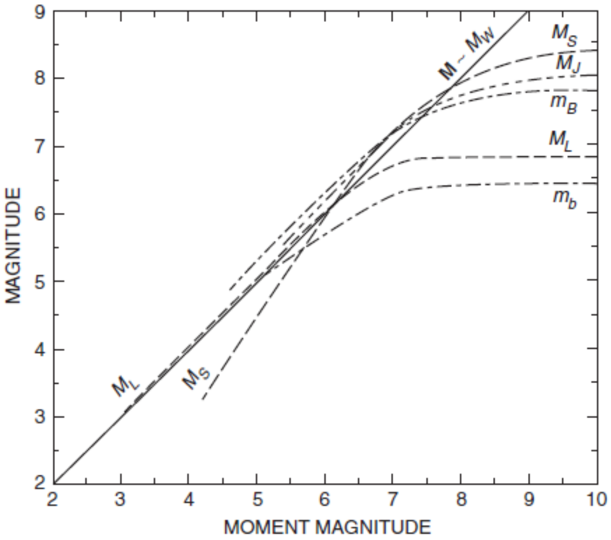

Figure 3. Relations between magnitude scales.

The range of periods of different magnitude scales is: for mb:~1 s; for M_L: ~0.1-3 s form mB: ~ 0.5-15 s; for M_s: ~ 20s and for Mw: ~10 - ∞. For shorter periods, early saturation occurs. For instance, m_b saturates around 6.5, M_L around 7, mB at 8 and M_s at about 8.5. Mw magnitude does not saturate [13].

3. Conclusions

Size of an earthquake is one of the most fundamental earthquake source parameters of seismic catalogs. A reliable size of an earthquake is essential for engineering, tectonic studies, seismic hazard and risk assessment applications. Earthquake size is the basis of a variety of scientific research. The size of earthquakes are characterized in two different ways; macroseismic intensity scale (I) and magnitude (M).

Macroseismic intensity represents strength of the event in terms of human perception, damage to buildings and changes in the surrounding environment.

Magnitude scale is a logarithmic measure of the size of an event derived from instrumental records. The size estimates of different magnitude scales may be different for the same earthquake due to the magnitude calculation methods. There is no scale limitation to magnitudes whereas macroseismic scale is limited to 10 or 12-degree scale. Different macroseismic scales can be used in different countries depending on the regional properties. Earthquake magnitude scale is not uniform due to changes in instrumentation, the data reduction method and the magnitude formula. Various magnitude scales have been developed. The magnitude scales change with the range of period of the signal used during magnitude determination. Seismic moment magnitude is one the most reliable, uniform type of non-saturating magnitude for earthquakes derived from seismic moment that uses source parameters of the earthquake region.

References

[1] Bormann P., Wendt S., DiGiacomo D., 2013. Seismic Sources and Source Parameters. In: Bormann P. (Ed.), New Manual of Seismological Observatory Practice 2 (NMSOP2), Potsdam, Germany. https://doi.org/10.2312/GFZ.NMSOP-2_ch3.

[2] Bormann P., 2011. Earthquakes, Intensity in Encyclopedia of Solid Earth Geophysics, Springer, Dordrecht, The Netherlands.

[3] Musson R. M., Cecić I., 2012. New Manual of Seismological Observatory Practice 2 (NMSOP-2). doi.org/10.2312/GFZ.NMSOP-2_ch12.

[4] Wald D. J., Quitoriano V., Heaton T. H., Kanamori H., 1999. Relationships Between Peak Ground Acceleration, Peak Ground Velocity, and Modified Mercalli Intensity in California. Earthquake Spectra, **15**(3), pp.557-564.

[5] Grünthal G., 2011. Earthquakes, Intensity in Encyclopedia of Solid Earth Geophysics, Springer, Dordrecht, The Netherlands.

[6] 24 Ocak 2020 Elazığ Sivrice Depremi Basın Bülteni, http://www.koeri.boun.edu.tr/sismo/2/wp-content/uploads/2020/01/24_Ocak_2020_Sivrice_Elazig_Depremi_V13.pdf. (Access Date: 23.10.2020).

[7] Richter C. F., 1935. An Instrumental Earthquake Magnitude Scale. Bulletin of the Seismological Society of America, **25**(1), pp.1-32.

[8] Kanamori H., 1977. The Energy Release in Great Earthquakes. Journal of Geophysical Research, **82**(20), pp.2981-2987.

[9] Kanamori H., Brodsky E. E., 2004. The Physics of Earthquakes. Reports on Progress in Physics, **67**(8), pp.1429

[10] Earthquake Glossary Seismic moment, https://earthquake.usgs.gov/learn/glossary/?term= seismic%20moment (Access Date: 24.10.2020).

[11] Campbell K.W., 1985. Strong Motion Attenuation Relations: a Ten-Year Perspective. Earthquake Spectra, **1**(4), pp.759-804.

[12] Kanamori H., 1983. Magnitude Scale and Quantification of Earthquakes. Tectonophysics, **93**(3-4), pp.185-199.

[13] Bormann P., 2002. Magnitude of Seismic Events. IASPEI New Manual of Seismological Observatory Practice, 1, pp.16-50.

Koc. J. Sci. Eng., 3(2): (2020) 59-63 https://doi.org/10.34088/kojose.797216

Kocaeli University

Kocaeli Journal of Science and Engineering

http://dergipark.org.tr/kojose

Equation Including Local Fractional Derivative and Neumann Boundary Conditions

Suleyman CETINKAYA [1,*], Ali DEMIR [2]

[1] *Department of Mathematics, Faculty of Arts and Sciences, Kocaeli, 41380, Turkey,* ***ORCID:*** *0000-0002-8214-5099*
[2] *Department of Mathematics, Faculty of Arts and Sciences, Kocaeli, 41380, Turkey,* ***ORCID:*** *0000-0003-3425-1812*

Article Info

Research paper

Received *: September 19, 2020*
Accepted *: November 23, 2020*

Keywords

Local Fractional Derivative
Neumann Boundary Conditions
Separation of Variables
Spectral Method

Abstract

The aim of this study to discuss the construction of solution of fractional partial differential equations (FPDEs) with initial and boundary conditions. Since the homogenous initial boundary value problem involves local fractional-order derivative, it has classical initial and boundary conditions. By means of the separation of variables method (SVM) and the inner product on $L^2[0,l]$, we construct the solution in this series form in terms of eigenfunctions of related Sturm-Liouville problem. An illustrative example presents the applicability and influence of separation of variables method on fractional mathematical problems.

1. Introduction

Since mathematical models including fractional derivatives play a vital role fractional derivatives draw the growing attention of many researchers in various branches of sciences. Therefore there are many different fractional derivatives such as Caputo, Riemann-Liouville, Atangana-Baleanu. However these fractional derivatives do not satisfy the most important properties of ordinary derivative which leads to many difficulties to analyze or obtain the solution of fractional mathematical models. As a result many scientists focus on defining new fractional derivatives to cover the setbacks of the defined ones. Moreover, the success of mathematical modelling of systems or processes depends on the fractional derivative, it involves, since the correct choice of the fractional derivative allows us to model the real data of systems or processes accurately.

In order to define new fractional derivatives, various methods exist and these ones are classified based on their features and formation such as nonlocal fractional derivatives and local fractional derivatives. The proportional derivative is a newly defined fractional derivative which is generally defined as

- ${}^{P}D_{\alpha} f(t) = K_1(\alpha,t)\, f(t) + K_0(\alpha,t) f'(t)$

where the functions K_0 and K_1 satisfy certain properties in terms of limit [1] and f is a differentiable function. Notice that this derivative can be regarded as an extension of conformable derivative and is used in control theory.

In this study we focus on obtaining the solution of the following fractional diffusion equation including various proportional derivative operator by making use of the separation of variables method:

- ${}^{P}D_t^{\alpha} u(x,t) = \gamma^2 u_{xx}(x,t),$
- $u_x(0,t) = u_x(l,t) = 0,$
- $u(x,0) = f(x)$

where $0 < \alpha < 1, 0 \le x \le l, 0 \le t \le T, \gamma \in R$. Here we use the following forms of the proportional derivatives:

$${}^{P}D_t^{\alpha} f(t) = K_1(\alpha)\, f(t) + K_0(\alpha) f'(t). \tag{1}$$

Especially we consider the following ones:

---

[*] Corresponding Author: suleyman.cetinkaya@kocaeli.edu.tr

- ${}_{1}^{P}D_t^{\alpha} f(t) = (1-\alpha)\, f(t) + \alpha f'(t)$ and
- ${}_{2}^{P}D_t^{\alpha} f(t) = (1-\alpha^2)\, f(t) + \alpha^2 f'(t)$

From a physical aspect, the intrinsic nature of the physical system can be reflected in the mathematical model of the system by using fractional derivatives. Therefore the solution of the fractional mathematical model is in excellent agreement with the predictions and experimental measurement of it. The systems whose behaviour is non-local can be modelled better by fractional mathematical models. Moreover, the degree of its non-locality can be arranged by the order of fractional derivative. In order to analyze the diffusion in a non-homogenous medium that has memory effects, it is better to analyze the solution of the fractional mathematical model for this diffusion. As a result in order to model a process, the correct choices of fractional derivative and its order must be determined.

In this study, local fractional derivative is used to model diffusion problems as in the case of non-local fractional derivative, models including local fractional derivatives give better results than models including integer order derivatives. In the mathematical modelling of diffusion problem for different matters such as liquid, gas and temperature, the suitable fractional order α is chosen, since the diffusion coefficient γ^2 depends on the order α of fractional derivative [2]. This mathematical modelling describes the behaviour of matter in a phase. There are many published works on the diffusion of various matters in science especially in fluid mechanics and gas dynamics [3-14]. From this aspect, analysis of this problem plays an important role in application. Moreover, sub-diffusion cases for which $0 < \alpha < 1$ are under consideration. The solution of the fractional mathematical model of sub-diffusion cases behaves much slower than the solution of the integer-order mathematical model unlike the fractional mathematical model for super-diffusion.

2. Main Results

Let us consider the following problem including the proportional derivative in Eq. (1)

$$ {}^{P}D_t^{\alpha} u(x,t) = \gamma^2 u_{xx}(x,t), \qquad (2)$$

$$ u_x(0,t) = u_x(l,t) = 0, \qquad (3)$$

$$ u(x,0) = f(x) \qquad (4)$$

where $0 < \alpha < 1, 0 \le x \le l, 0 \le t \le T, \gamma \in R$.

By employing SVM, the solution of the problem in Eqs. (2-4) can be written in the following form:

$$ u(x,t;\alpha) = X(x)\, T(t;\alpha) \qquad (5)$$

where $0 \le x \le l,\ 0 \le t \le T$. Plugging Eq. (5) into Eq. (2) and arranging it, we have

$$ \frac{{}^{P}D_t^{\alpha}(T(t;\alpha))}{T(t;\alpha)} = \gamma^2 \frac{X^{11}(x)}{X(x)} = -\lambda^2 \qquad (6)$$

By taking the last equality from Eq. (6) and utilizing the boundary conditions in Eq. (3), we have the following problem:

$$ X^{11}(x) + \lambda^2 X(x) = 0, \qquad (7)$$

$$ X^{1}(0) = X^{1}(l) = 0. \qquad (8)$$

The problem in Eq. (7-8) is the well known Sturm-Liouville problem. The solution to this problem is as in Eq. (9):

$$ X_n(x) = \cos\left(w_n\left(\frac{x}{l}\right)\right), n = 0,1,2,3,\ldots \qquad (9)$$

where $w_n = n\pi, n = 0,1,2,3,\ldots$ satisfy the equation $sin(w_n) = 0$ and $\lambda_n = \frac{w_n}{l}, \lambda_1 < \lambda_2 < \lambda_3 < \cdots, n = 0,1,2,3,\ldots.$

The second equation in Eq. (6) for eigenvalue λ_n yields the fractional differential equation below:

- $\frac{{}^{P}D_t^{\alpha}(T(t;\alpha))}{T(t;\alpha)} = -\gamma^2\lambda_n^2,$
- $\frac{K_1(\alpha)\, T_n(t;\alpha) + K_0(\alpha) T_n^1(t;\alpha)}{T_n(t;\alpha)} = -\gamma^2\lambda_n^2,$
- $K_0(\alpha) T_n^1(t;\alpha) + \left(\gamma^2\lambda_n^2 + K_1(\alpha)\right) T_n(t;\alpha) = 0,$

which yields the following solution

- $T_n(t;\alpha) = exp\left(-\frac{\gamma^2\lambda_n^2 + K_1(\alpha)}{K_0(\alpha)} t\right), n = 0,1,2,3,$

The solution for every eigenvalue λ_n is constructed as

- $u_n(x,t;\alpha) = X_n(x) T_n(t;\alpha) =$
  $exp\left(-\frac{\gamma^2\lambda_n^2 + K_1(\alpha)}{K_0(\alpha)} t\right) \cos\left(w_n\left(\frac{x}{l}\right)\right), n = 0,1,2,3,$

which leads to the following general solution

$$ u(x,t;\alpha) = A_0 + \sum_{n=1}^{\infty} A_n \cos\left(w_n\left(\frac{x}{l}\right)\right) exp\left(-\frac{\gamma^2\lambda_n^2 + K_1(\alpha)}{K_0(\alpha)} t\right). \qquad (10)$$

Note that it satisfies boundary conditions and fractional differential equation. If γ^2 is replaced by the fractional diffusion coefficient $c^2\tau_\alpha^{1-\alpha}$ where c^2 is ordinary diffusion coefficient and τ_α is a time constant the solution takes the following form:

- $u(x,t;\alpha) = A_0 + \sum_{n=1}^{\infty} A_n \cos\left(w_n\left(\frac{x}{l}\right)\right) exp\left(-\frac{c^2\tau_\alpha^{1-\alpha}\lambda_n^2+K_1(\alpha)}{K_0(\alpha)}t\right).$

The coefficients of the general solution are established by taking the following initial condition into account:

- $u(x,0) = f(x) = A_0 + \sum_{n=1}^{\infty} A_n \cos\left(w_n\left(\frac{x}{l}\right)\right).$

The coefficients A_n for $n = 0,1,2,3, \dots$ determined by the help of inner product defined on $L^2[0,l]$:

- $A_0 = \frac{1}{l}\int_0^l f(x)dx,$
- $A_n = \frac{2}{l}\int_0^l f(x)\cos\left(w_n\left(\frac{x}{l}\right)\right).$

3. Illustrative Examples

Now the obtained results are illustrated by two examples in this part. Let the Neumann boundary value problem below be taken into account:

$$u_t(x,t) = u_{xx}(x,t), \tag{11}$$

$$u_x(0,t) = 0,\ u_x(1,t) = 0, \tag{12}$$

$$u(x,0) = \cos(\pi x) \tag{13}$$

whose solution is established as:

- $u(x,t) = \cos(\pi x)\, e^{-\pi^2 t}$

where $0 \le x \le 1, 0 \le t \le T.$

Example 1. Now let the following problem called fractional heat-like problem be taken into consideration:

$$\begin{aligned} &{}_1^PD_t^\alpha u(x,t) = u_{xx}(x,t),\\ &u_x(0,t) = 0,\ u_x(1,t) = 0,\\ &u(x,0) = \cos(\pi x) \end{aligned} \tag{14}$$

where $0 < \alpha < 1, 0 \le x \le 1,\ 0 \le t \le T$. It is clear from Eq. (10) that the solution to the above problem can be obtained in the following form:

$$u(x,t;\alpha) = A_0 + \sum_{n=1}^{\infty} A_n \cos(n\pi x)\, exp\left(-\frac{n^2\pi^2+1-\alpha}{\alpha}t\right) \tag{15}$$

Plugging $t = 0$ into the solution in Eq. (15) and utilizing the initial condition in Eq. (14) leads to:

- $\cos(\pi x) = A_0 + \sum_{n=1}^{\infty} A_n \cos(n\pi x)$

The coefficients A_n for $n = 0,1,2,3, \dots$ are determined by the help of the inner product as follows:

- $A_0 = 0.$

For $n \neq 1, A_n = 0. n = 1$ we get

- $A_1 = 1.$

Thus

$$u(x,t;\alpha) = \cos(\pi x)\, exp\left(-\frac{\pi^2+1-\alpha}{\alpha}t\right). \tag{16}$$

It is clear that taking $\alpha = 1$ in Eq. (16) leads to the solution of the problem (Eqs. (11-13)) which implies the correctness of the method employed in this study.

Example 2. Now let the following problem called fractional heat-like problem be taken into consideration:

- ${}_2^PD_t^\alpha u(x,t) = u_{xx}(x,t),$
- $u_x(0,t) = 0,\ u_x(1,t) = 0,$
- $u(x,0) = \cos(\pi x)$

where $0 < \alpha < 1, 0 \le x \le 1,\ 0 \le t \le T$. It is clear from Eq. (10) that the solution to the above problem can be obtained in the following form:

- $u(x,t;\alpha) = A_0 + \sum_{n=1}^{\infty} A_n \cos(n\pi x)\, exp\left(-\frac{\gamma^2\lambda_n^2+1-\alpha^2}{\alpha^2}t\right).$

As in Example 1, after similar computations the solution can be constructed as follows:

- $u(x,t;\alpha) = \cos(\pi x)\, exp\left(-\frac{\pi^2+1-\alpha^2}{\alpha^2}t\right).$

The graphics of solutions for Example 1, Example 2, and the problem (Eqs. (11-13)) in 2D and 3D are given in Figure 1 and Figure 2 respectively.

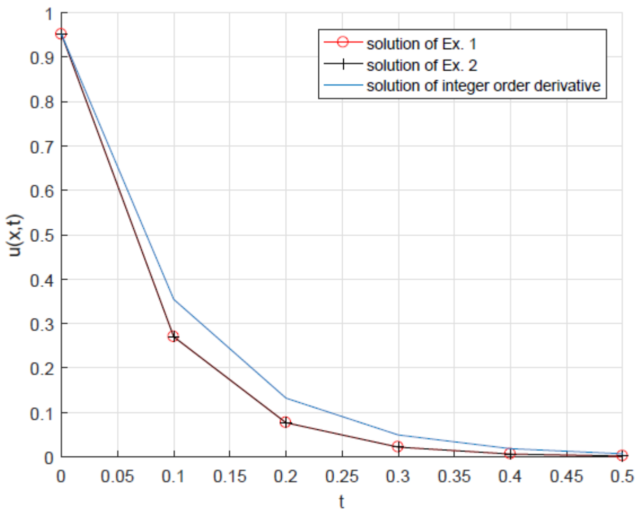

Figure 1. The graphics of solutions for Example 1 and Example 2 in 2D at $x = 0.1$ for α = 0.8.

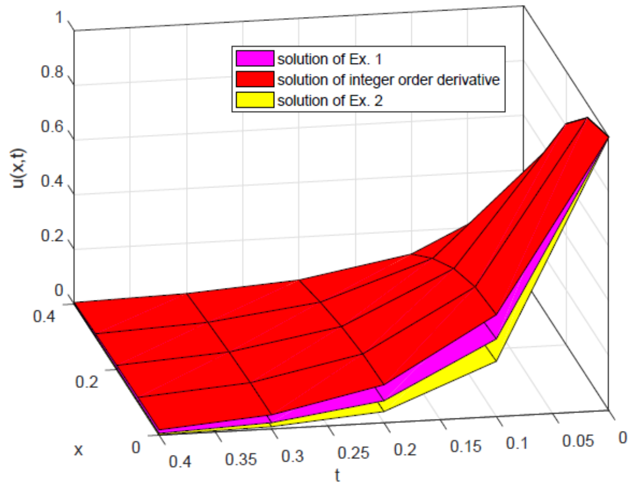

Figure 2. The graphics of solutions for Example 1 and Example 2 in 3D for α = 0.8.

4. Conclusion

In this investigation, the solution of the diffusion problem including local time-fractional derivatives in one dimension is constructed analytically in the series form. Taking the SVM into account, the solution is formed in the form of a series in terms of the eigenfunctions of a related Sturm-Liouville problem including fractional derivative in a proportional sense.

Based on the analytic solution, we reach the conclusion that diffusion processes decay exponential with time until initial condition is reached. As α tends to 0, the rate of decay increases. This implies that in the mathematical model for diffusion of the matter which has a small diffusion rate the value of α must be close to 0. This model can account for various diffusion processes of various methods.

References

[1] Dumitru B., Arran F., Akgül A., 2020. On a Fractional Operator Combining Proportional and Classical Differintegrals. Mathematics, **8**(360). doi:10.3390/math8030360

[2] Bisquert J., 2005. Interpretation of A Fractional Diffusion Equation with Nonconserved Probability Density in Terms of Experimental Systems with Trapping or Recombination. Physical Review E, **72**. doi: 10.1103/PhysRevE.72.011109

[3] Ndolane S., 2019. Solutions of Fractional Diffusion Equations and Cattaneo-Hristov Diffusion Model. International Journal of Analysis and Applications, **17**(2), pp. 191-207. doi: 10.28924/2291-8639-17-2019-191

[4] Aguilar J. F. G., Hernández M. M., 2014. Space-Time Fractional Diffusion-Advection Equation with Caputo Derivative. Abstract and Applied Analysis. **2014** doi: 10.1155/2014/283019

[5] Naber M., 2004. Distributed order fractional sub-diffusion. Fractals, **12**(1), pp. 23-32. doi: 10.1142/S0218348X04002410

[6] Nadal E., Abisset C. E., Cueto E., Chinesta F., 2018. On the Physical Interpretation of Fractional Diffusion. Comptes Rendus Mecanique, **346**, pp. 581-589. doi: 10.1016/j.crme.2018.04.004

[7] Zhang W., Yi M., 2016. Sturm-Liouville Problem and Numerical Method of Fractional Diffusion Equation on Fractals. Advances in Difference Equations, **2016:217**. doi: 10.1186/s13662-016-0945-9

[8] Cetinkaya S., Demir A., Kodal Sevindir H., 2020. The Analytic Solution of Initial Boundary Value Problem Including Time-fractional Diffusion Equation. Facta Universitatis Ser. Math. Inform, **35**(1), pp. 243-252.

[9] Cetinkaya S., Demir A., Kodal Sevindir H., 2020. The Analytic Solution of Sequential Space-time Fractional Diffusion Equation Including Periodic Boundary Conditions. Journal of Mathematical Analysis, **11**(1), pp. 17-26.

[10] Cetinkaya S., Demir A., 2019. The Analytic Solution of Time-Space Fractional Diffusion Equation via New Inner Product with Weighted Function. Communications in Mathematics and Applications, **10**(4), pp. 865-873.

[11] Cetinkaya S., Demir A., Kodal Sevindir H., 2020. The Analytic Solution of Initial Periodic Boundary Value Problem Including Sequential Time Fractional Diffusion Equation. Communications in Mathematics and Applications, **11**(1), pp. 173-179.

[12] Cetinkaya S., Demir A., Time Fractional Equation Including Non-homogenous Dirichlet Boundary Conditions. Sakarya University Journal of Science (Accepted Paper).

[13] Cetinkaya S., Demir A., Sequential Space Fractional Diffusion Equation's solutions via New Inner Product. Asian-European Journal of Mathematics (Accepted Paper). doi: 10.1142/S1793557121501217

[14] Cetinkaya S., Demir A., Time Fractional Diffusion Equation with Periodic Boundary Conditions. Konuralp Journal of Mathematics, **8**(2)**,** pp. 337-342.

KOCAELI UNIVERSITY

1992